Gardening of the Martian Regolith by Diurnal CO2 Frost and the Formation of Slope Streaks

Lucas Lange[1], Sylvain Piqueux[2], and 0000-0002-8096-9633 Christopher Edwards[3]

[1]SSPA, Institut Supérieur de l'Aéronautique et de l'Espace (ISAE-SUPAERO), Université de Toulouse, 31400, Toulouse, France. Now at Laboratoire de Météorologie Dynamique, Institut Pierre-Simon Laplace (LMD/IPSL), Sorbonne Université, Centre National de la Recherche Scientifique (CNRS), École Polytechnique, École Normale Supérieure (ENS), Paris, France
[2]Jet Propulsion Laboratory, California Institute of Technology, Pasadena, CA 91109, USA
[3]Northern Arizona University, Department of Astronomy and Planetary Science PO BOX 6010 Flagstaff, AZ 86011, US

November 22, 2022

Abstract

Before dawn on the dustiest regions of Mars, surfaces measured at or below 148 K are common. Thermodynamics principles indicate that these terrains must be associated with the presence of CO2 frost, yet visible wavelength imagery does not display any ice signature. We interpret this systematic absence as an indication of CO2 crystal growth within the surficial regolith, not on top of it, forming hard-to-distinguish intimate mixtures of frost and dust, i.e., dirty frost. This particular ice/regolith relationship unique to the low thermal inertia regions is enabled by the large difference in size between individual dust grains and the peak thermal emission wavelength of any material nearing 148 K (1-2 μm vs. 18 μm), allowing radiative loss (and therefore ice formation) to occur deep within the pores of the ground, below several layers of grains. After sunrise, sublimation-driven winds promoted by direct insolation and conduction create an upward drag within the surficial regolith that can be comparable in strength to gravity and friction forces combined. This drag displaces individual grains, possibly preventing their agglomeration, induration, and compaction, and can potentially initiate or sustain downslope mass movement such as slope streaks. If confirmed, this hypothesis introduces a new form of CO2-driven geomorphological activity occurring near the equator on Mars and explains how large units of mobile dust are currently maintained at the surface in an otherwise soil-encrusting world.

Gardening of the Martian Regolith by Diurnal CO_2 Frost and the Formation of Slope Streaks

L.Lange[1,2], S.Piqueux[3], and C.S.Edwards[4]

[1]SSPA, Institut Supérieur de l'Aéronautique et de l'Espace (ISAE-SUPAERO), Université de Toulouse, 31400, Toulouse, France
[2]Now at Laboratoire de Météorologie Dynamique, Institut Pierre-Simon Laplace (LMD/IPSL), Sorbonne Université, Centre National de la Recherche Scientifique (CNRS), École Polytechnique, École Normale Supérieure (ENS), Paris, France
[3]Jet Propulsion Laboratory, California Institute of Technology, Pasadena, CA 91109, USA
[4]Northern Arizona University, Department of Astronomy and Planetary Science PO BOX 6010 Flagstaff, AZ 86011, USA

Key Points:

- Near dawn, diurnal frost is not apparent on cold, dusty, low thermal inertia terrains;
- These observations are consistent with a model of dirty diurnal CO_2 frost, fluffing up the surface layer when it sublimes;
- This mechanism could trigger dynamic phenomena on the Martian surface and lead to the formation of slope streaks.

Corresponding author: Sylvain Piqueux, sylvain.piqueux@jpl.nasa.gov

Abstract

Before dawn on the dustiest regions of Mars, surfaces measured at or below ~ 148 K are common. Thermodynamics principles indicate that these terrains must be associated with the presence of CO_2 frost, yet visible wavelength imagery does not display any ice signature. We interpret this systematic absence as an indication of CO_2 crystal growth within the surficial regolith, not on top of it, forming hard-to-distinguish intimate mixtures of frost and dust, i.e., dirty frost. This particular ice/regolith relationship unique to the low thermal inertia regions is enabled by the large difference in size between individual dust grains and the peak thermal emission wavelength of any material nearing 148 K (1-2 μm vs. 18 μm), allowing radiative loss (and therefore ice formation) to occur deep within the pores of the ground, below several layers of grains. After sunrise, sublimation-driven winds promoted by direct insolation and conduction create an upward drag within the surficial regolith that can be comparable in strength to gravity and friction forces combined. This drag displaces individual grains, possibly preventing their agglomeration, induration, and compaction, and can potentially initiate or sustain downslope mass movement such as slope streaks. If confirmed, this hypothesis introduces a new form of CO_2-driven geomorphological activity occurring near the equator on Mars and explains how large units of mobile dust are currently maintained at the surface in an otherwise soil-encrusting world.

Plain Language Summary

Surface CO_2 ice forms at all latitudes on Mars, with a strong seasonal control. In this study, we show that diurnal CO_2 ice is not observed in visible wavelength imagery in dusty terrains, where diurnal frost preferentially forms. We interpret this situation as the indication of the presence of hard-to-distinguish dirty frost, where ice crystals grow within the surficial regolith, not on top of it, resulting in apparent soil-like dark ice. At sunrise, sublimation-driven winds within the regolith are occasionally strong enough to displace individual dust grains, initiating and sustaining dust avalanches on steep slopes, forming ground features known as slope streaks. This model suggests that the CO_2 frost cycle is an active geomorphological agent at all latitudes and not just at high or polar latitudes, and possibly a key factor maintaining mobile dust reservoirs at the surface.

1 Introduction

The seasonal transfer of CO_2 between the atmosphere and the surface at high latitudes is associated with a wide range of exotic processes shaping the surface morphology (Diniega et al., 2021, 2013; Dundas et al., 2012; Hansen et al., 2013; Pilorget & Forget, 2015; Piqueux et al., 2003; Piqueux & Christensen, 2008), the composition of the atmosphere (Sprague et al., 2004, 2007), impacting the global climate and weather (Haberle, 1979; Haberle et al., 1979; Hourdin et al., 1993), and possibly degrading the near-surface climate record stored in the polar layered deposits (Kieffer et al., 2006; Kieffer, 2007). In contrast, the existence and ubiquity of a diurnal CO_2 cycle at mid and low-latitudes has only recently been exposed (Piqueux et al., 2016; Khuller et al., 2021a). Its impact on the physical state of the regolith, if any, is speculative although Mischna and Piqueux (2020) and Piqueux et al. (2016) proposed that it could take different forms, including initiating slope streaks (Schorghofer et al., 2002, 2007), preventing widespread dust induration/duricrust formation, and influencing the global environment over long periods of time through the nurturing of a global reservoir of mobile dust able to be lifted in the atmosphere.

Piqueux et al. (2016) suggest that the recurring diurnal growth and sublimation of CO_2 crystals could indeed cryoturb the very surficial regolith because frost should be

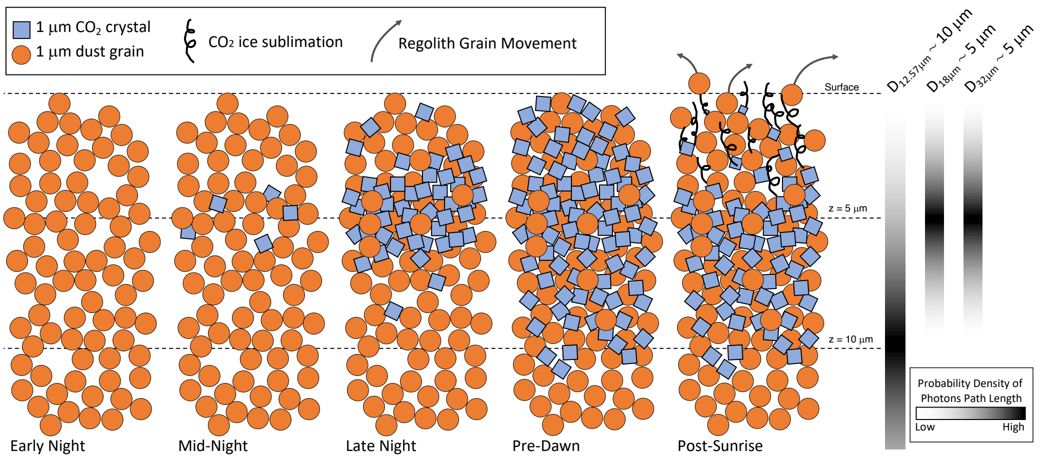

Figure 1. Schematic model of the CO_2 frost (blue squares) and regolith dust grains (orange circles) relationship in dusty low thermal inertia regions, and its evolution throughout a night and sunrise. Approximate conceptual penetration depths computed with Eq. (1) (without scattering) are indicated on the right and figurated as a shade of grey: $D_{18\mu m}$ peaks at 5 μm and corresponds to the typical distance traveled by photons at a wavelength $\lambda = 18$ μm (i.e., peak radiative loss for material approaching T_{CO_2}); $D_{12.57\mu m}$ peaks near 10 μm and corresponds to the typical distance traveled by photons detected by THEMIS (band 9); $D_{32\mu m}$ peaks near 5 μm and corresponds to the typical distance traveled by photons detected by MCS (channel B1). Frost crystals and regolith grains are approximately 1 μm in size to conform with various observations (Lemmon et al., 2019; Piqueux et al., 2016) and laboratory work (Presley & Christensen, 1997). In this model, the surficial regolith is free of diurnal frost at the beginning of the night ("Early Night"); when the surface approaches $\sim$ 148 K, the peak radiative loss occurs at $\lambda = 18$ μm (Wien's law) with photons emerging from $\sim$ 5 μm depth (see Eq. (1) and associated text), where ice crystals are predicted to form first resulting in dirty frost ("Mid-Night"); radiative loss continues during the night, forming more CO_2 ice, preferentially at 5 μm depths ("Late Night"), and eventually in shallower and deeper layers ("Pre-Dawn") until the end of the night. At sunrise, CO_2 ice sublimates, creating an upward sublimation-driven wind that could lead to grain displacement.

present in the pores of the regolith, not exclusively on top of it. This model of diurnal ice forming within the pores of the regolith is supported by the following two arguments:

- Low-latitude CO_2 frost-like surface temperatures have been identified at night in low thermal inertia terrains using Mars Climate Sounder (MCS, (McCleese et al., 2007)) data acquired in the thermal infrared at $\sim$ 32 μm (Piqueux et al., 2016), and Thermal Emission Imaging System (THEMIS, Christensen et al. (2004)) data acquired at 12.57 μm (Khuller et al., 2021a). At these wavelengths, the penetration depths D_λ [m] (i.e., the distance traveled by photons in the regolith at a given wavelength λ[m]) are up to one order of magnitude longer than the typical regolith grain size where frost is observed (1-2 μm for atmospherically sedimented material found in these low thermal inertia regions (Lemmon et al., 2019; Presley & Christensen, 1997)). These depths ignore scattering and are estimated using the inverse of k (i.e., the imaginary part of the refractive index of dust given by Wolff et al. (2006)), following Eq. (1) (Hansen, 1997):

$$D_\lambda = \frac{\lambda}{4\pi k} \quad (1)$$

At THEMIS and MCS wavelengths, $D_{12.57\mu m}$ and $D_{32\mu m}$ computed with Eq. (1) peak at 5 and 10 μm using $k \approx 0.1$ and $k \approx 0.45$, respectively. These penetration depths are up to one order of magnitude longer than the typical regolith grain size where frost is observed (1-2 μm (Lemmon et al., 2019; Presley & Christensen, 1997)). As such, the photons captured by the MCS and THEMIS detectors indicate that CO_2 frost-like surface temperatures are present at least within the top few microns to tens of microns of the regolith, that is, within a regolith layer that is characterized by several dust grains in thickness. For this reason, these MCS and THEMIS observations show that temperatures conducive to diurnal CO_2 ice formation exist within a surface layer that is many regolith grains thick, and not exclusively on top of it. Again, this reasoning only holds for very low thermal inertia regions associated with very small and loose regolith grains, and those happen to be the ones displaying overnight CO_2 ice-like temperatures (Piqueux et al., 2016; Khuller et al., 2021a);

- Wien's displacement law indicates that the peak infrared emission for $\sim$ 148 K surfaces, i.e., the average CO_2 ice temperature on Mars (Leighton & Murray, 1966) is $\sim$ 18 μm. This is the typical wavelength of photons emitted by a surface about to -or already in the process of- forming, or losing, CO_2 ice. From Eq. (1) and using $k \approx 0.35$ (Wolff et al., 2006), $D_{18\mu m}$ is in the order of 5 microns when neglecting scattering, that is, many regolith grains in thickness. As such, the surface layer is preferentially cooling/radiating energy from "within" multiple layers of regolith grains, not at the very top as would be the case with larger grains, and the lowest regolith temperatures may not always be encountered at the very surface, but a few grains deep. This configuration is somewhat analogous to models predicting peak daytime temperatures away from the topmost surface (Henderson & Jakosky, 1994), although the process involved here is different. As mentioned above, these photons associated with a wavelength $\lambda \sim 18$ μm can freely travel through such thin dust layers, confirming that energy is lost many grains below the surface without reabsorption on the way out. A word of caution about the length of the optical paths for thermal infrared photons calculated with Eq. (1) and reported in this paper: they could correspond to an upper limit as scattering should reduce these distances. A formal calculation of the effect of scattering in the model proposed in Fig. 1 is difficult because of the complex geometrical relationship between ice crystals and dust grains, requiring advanced radiative modeling not performed as part of this work. But because of the significant amount of dust inherent to our dirty frost model, the optical properties of the dust grains are dominant in the resulting ice-dust mixture (Kieffer 2007, Langevin et al. 2006, Fig. 6 from Pilorget et al., 2011), and laboratory experiments have demonstrated that at thermal-infrared wavelengths, photons can penetrate thick (i.e., tens of micrometers) analog/terrestrial dust layers (Christensen & Harrison, 1993; Christensen et al., 2004; Ramsey & Christensen, 1992; Johnson et al., 2002), even larger than those reported in Fig. 1.

  We conclude that in very low thermal inertia terrains only, CO_2 frost is anticipated to form in the pores of the regolith below a few dust grains (or deeper), resulting in mixtures of dust and frost, referred to in this paper as icy regolith or dirty frost. Of course, when the regolith thermal inertia is associated with grains much larger than a few microns in size (thermal inertia > 100 J m^{-2} K^{-1} s$^{-1/2}$, Presley and Christensen (1997)), individual regolith grains are large enough to contribute individually to the surface thermal emission, and ice shall form on the surface of these uppermost grains.

Fig. 1 provides a schematic view of this proposed dirty frost model. After the sun sets ("Early Night"), the surface temperature is above T_{CO_2} and no ice is present. Conduction and radiative cooling compete near the surface, but the very low thermal conductivity in the low thermal inertia regions observed near the Equator on Mars results in rapid cooling of the surface. The peak radiative loss occurs at $\lambda \sim 18$ μm and is associated with photons typically emitted between from 5 μm in depth (see discussion above). When the temperature reaches T_{CO_2}, the first crystals form at these depths in the pores of the regolith ("Mid-Night"). Radiative loss continues, but the minimum kinetic temperature does not drop below T_{CO_2}. Instead, more CO_2 ice forms in the pores, still preferentially near 5 μm in depth ("Late Night"). Thermal infrared spectroscopy indicates that the CO_2 crystals are ~ 1 μm in size (Piqueux et al., 2016). Cooling through conduction and radiation bleeds to other depths, leading to the formation of CO_2 ice in the pores at other depths ("Pre-Dawn", with dawn loosely defined in this model as the late night time period, before the sun rises, when some light illuminates the surface and allows visible wavelength imagery acquisition with THEMIS showing surface features). Energy and mass balance modeling shows that CO_2 ice typically condenses equivalent thicknesses of a few tens of microns in the form of micrometer size ice crystals (Piqueux et al., 2016), and the very porous substrate associated with low inertia terrains (Presley & Christensen, 1997) implies that the ice to dust ratio should be measured in %, if not 10's of %, but certainly not at the contamination level. One consequence is that the visible wavelength albedo of this thin dusty ice unit should be that of the bare dust (Singh & Flanner, 2016; Warren et al., 1990).

This model predicts that surface temperatures associated at sunrise with T_{CO_2} in low thermal inertia terrains should not display any signature of ice in imagery of the ground, in contrast with other terrains at T_{CO_2} but associated with higher thermal inertia values. Consequently, we hypothesize that diurnal CO_2 frost associated with dusty low thermal inertia surfaces should be exceedingly difficult to identify in visible wavelength imagery, in contrast with diurnal or seasonal CO_2 frost present elsewhere on Mars in terrains where the surface material consists on larger regolith grains. Note that this model is not predicted to apply to the polar regions where low thermal inertia deposits are not observed. In this paper, we present an analysis of THEMIS data acquired near sunrise at both visible and thermal infrared wavelengths in order to constrain the nature of the frost/regolith relationship on dusty terrains on Mars and test the dirty frost model (Fig. 1).

In addition, one potential implication for this recurring diurnal growth and sublimation of CO_2 frost crystals within low thermal inertia terrains may include regular overnight surficial mechanical disruption of the soil, and possible fluffing by vertical sublimation-driven winds. This process could maintain high regolith porosity, and prevent compaction or inter-grain induration/cementation that seems to be ubiquitous elsewhere on Mars (Jakosky & Christensen, 1986; Mellon et al., 2000) except in low inertia terrains (Piqueux & Christensen, 2009a, 2009b; Putzig et al., 2005). Such recurring mechanical alteration of the regolith has been proposed as a process maintaining mobile dust available for lifting (Piqueux et al., 2016) contributing to impact the global climate over long periods of time (Mischna & Piqueux, 2020). Similar conclusions can been drawn when translucent ice forms on (or within) the Martian regolith: at sunrise, the solar energy is deposited at the base of the transparent frost layer, at the interface with the regolith grains, not at the very atmosphere/ground interface (see the abundant literature on the topic for the polar regions (Diniega et al., 2013, 2021; Hansen et al., 2010, 2013; Pilorget et al., 2013; Pilorget & Forget, 2015; Pilorget et al., 2011; Piqueux et al., 2003; Piqueux & Christensen, 2008; Piqueux et al., 2016; Pommerol et al., 2011; Pommerol et al., 2013; Portyankina et al., 2010, 2012; Thomas et al., 2010)). Basal sublimation yields winds internal to the very surficial regolith, and has the potential to disturb the upper regolith.

Another potential implication of this regolith gardening model that sets individual grains in motion at sunrise could be the initiation of dynamic surface mechanisms leading to the formation of slope streaks. Slope streaks are dark wedge-shaped surface features on sloped terrains, associated with downslope mass movement (Chuang et al., 2007; Ferris et al., 2002; Kreslavsky & Head, 2009; Miyamoto et al., 2004; Phillips et al., 2007; Schorghofer et al., 2002, 2007; Sullivan et al., 2001) that form exclusively in dusty low thermal inertia terrains. The initiating and sustaining mechanisms of slope streaks has been attributed to wet (Kreslavsky & Head, 2009; Mushkin et al., 2010; Schorghofer et al., 2002) or dry processes (Baratoux et al., 2006; Burleigh et al., 2012; Chuang et al., 2007, 2010; Dundas, 2020; Phillips et al., 2007; Schorghofer et al., 2002; Sullivan et al., 2001), without conclusive evidence one way or the other (Bhardwaj et al., 2019; Dundas, 2020). The longer-than-expected character of slope streaks on shallow Martian slopes requires some form of lubricating agent that has led Piqueux et al. (2016) to propose a connection with diurnal CO_2 ice sublimation grain motions, and slope destabilization. We hypothesize the existence of a spatial and temporal relationship between the presence of diurnal frost and the formation of slope streaks. The temporal relationship has been explored by Heyer et al. (2019) and is inconclusive, mainly because of the difficulty to determine the time of formation of slope streaks on images acquired infrequently from orbit. In this paper, we present an additional analysis of the spatial relationship between slope streaks distribution and diurnal frost presence.

The existence of a diurnal mechanical cycle within the surficial regolith associated with the growth and sublimation of CO_2 ice crystals would have significant geomorphological implications, including for equatorial terrains. The work presented in this paper aims at characterizing this relationship through visible and infrared wavelength imagery analysis, surface features mapping, and numerical modeling.

2 Methods

2.1 CO_2 Frost Optical Properties in Dusty Terrains

The optical properties of CO_2 ice (albedo and emissivity) have been extensively studied (Hansen, 1997; Schmitt et al., 1998) because of their control on local and global processes, from the condensation of the atmosphere (Forget et al., 1995; Forget & Pollack, 1996; Forget et al., 1998; Colaprete & Toon, 2002; Hayne et al., 2012, 2014) to the basal sublimation and venting of the caps (Piqueux et al., 2003; Kieffer et al., 2006; Pilorget et al., 2011).

Piqueux et al. (2016) demonstrated that thin layers (i.e., a few microns to tens of microns in thickness) of micrometer size ice crystals (as opposed to translucent slab-like ice) best match the high emissivities derived from MCS data in the low thermal inertia dusty units. Their conclusion is further supported by energy and mass balance modeling results suggesting that condensation involves up to a few hundreds of microns of CO_2 ice in thickness, much too small to form large translucent and high emissivity crystals (i.e., centimeters in sizes, (Kieffer, 2001, 2007; Kieffer et al., 2000; Langevin et al., 2006).

Here, we add that the high emissivities derived from the MCS observations at 32 μm are also consistent with frost forming within the uppermost pores of the regolith, and not just on top of it as these authors proposed. The surface emissivity is highly sensitive to the presence of frost at $\lambda \sim 12.57$ μm (THEMIS band 9, (Christensen et al., 2004)), even when it forms thin layers: ice thicknesses in the order of tens and hundreds of microns should result in a noticeable decrease of the surface emissivity, from ~ 0.96 to ~ 0.9-0.6 (Piqueux et al., 2016). While this reduction of the emissivity is magnified by the high emission angles considered for the MCS observations in the work present by Piqueux et al. (2016), (i.e., 70° vs. 0° for THEMIS), we can still reasonably assume that frost forming on the top of the regolith should measurably lower the emissivity compared to an ice-free surface. In contrast, frost forming within the pores, in other words highly dust-contaminated ice, should lead to surface emissivity approximately equal to the emissivity of ice-free dusty terrain ($\sim$0.96, (Ruff & Christensen, 2002; Piqueux et al., 2016)).

In this paper we present an analysis of the surface emissivity to further constrain the frost/regolith relationship in the low thermal inertia regions of Mars.

Micrometer size CO_2 ice crystals are associated with high albedo values at visible wavelengths (Hansen, 1997; Kieffer et al., 2000; Titus et al., 2008; Appéré et al., 2011; Singh & Flanner, 2016), but dust contamination can drastically reduce it (Kieffer et al., 2000; Murchie et al., 2019; Singh & Flanner, 2016; Warren et al., 1990). For this reason, the albedo (or color) of frosted terrains provides an excellent diagnostic tool of the relationship between the ice and the regolith grains, as intimate mixtures of ice and dust will be associated with dust-like albedo values, whereas clean ice layers on top of the surface dust will be characterized by high albedo values. As a word of caution, the references mentioned hereabove generally focus on dust contamination with large ice crystals, typically hundreds of microns in size or more, relevant to the polar regions (Kieffer et al., 2000). This large difference with the ice crystal sizes we consider in this work may not be inconsequential as Kieffer et al. (2000) report that the impact of dust contamination on albedo for ice crystals smaller than 10 μm can be more limited. We can expect that even with significant dust mixed in, very small and bright ice crystals placed on the top of the dust grains still display high albedo values (0.7-0.9) compared to ice-free ground (i.e., 0.27, Putzig et al. (2005)). Furthermore, Singh and Flanner (2016) show that the smaller the CO_2 ice crystals, the smaller the thickness of frost needed to contrast with a frost-free surface. Even for the relatively thin diurnal frost layers anticipated in the Martian mid latitudes of just a few tens of microns, an extrapolation of Singh and Flanner (2016)'s results (their Fig. 6) suggest high albedo values for the very small crytal sizes expected here (i.e., ~ 1 μm based on Piqueux et al. (2016)).

For all these reasons, we conclude that CO_2 frost layers 10's to 100's μm in thickness composed of clean ~ 1 μm crystals forming on the top of dusty surfaces are expected to yield a signature at visible wavelengths with a spectral slope from blue to red (Murchie et al., 2019), that is, blue(ish) pixels, similar to configurations observed on the seasonal caps (Calvin et al., 2015, 2017), and low emissivities at 12.57 μm. In contrast, CO_2 frost layers 10's to 100's μm in thickness mixed within the pores of the dusty regolith in the low thermal inertia terrains are expected to remain free of albedo contrast at visible wavelengths compared to unfrosted terrains and associated with high dust-like emissivity at 12.57 μm. In this paper, we leverage this difference of behavior to characterize the relationship between diurnal CO_2 frost and surface dust and test whether this frost forms on the regolith or within the pores.

2.2 Dataset and Frost Identification

To identify the presence of CO_2 ice and characterize its optical properties in dusty terrains, we use coincident visible and temperature observations acquired by THEMIS, a multispectral visible and thermal infrared wavelength imager observing the surface and atmosphere of Mars at various local times depending on the phase of the mission. THEMIS visible wavelength images form a smaller footprint than the thermal infrared images (~ 18 vs. ~ 32 km wide swath on the ground), so the infrared data is cropped to the extent of the overlapping visible wavelength data where the analysis is carried out. Henceforth, we do not consider or discuss THEMIS thermal infrared data where simultaneous visible wavelength observations are not available.

We only analyze data acquired near sunrise, when adequate lighting allows the acquisition of multiband visible wavelength imagery of the ground, and when diurnal frost is not only expected to be present, but near peak thickness, up to several hundreds of microns (Piqueux et al., 2016). We select data acquired at high incidence angles i, e.g., $70° < i < 110°$ (with $i < 90°$ indicating the Sun above the horizon, $i = 90°$ the Sun at the horizon, and $i > 90°$ the Sun below the horizon). Such data were thus acquired typically between 6 - 8 A.M. and 5 - 6 P.M. (Local True Solar Time -LTST-). Obser-

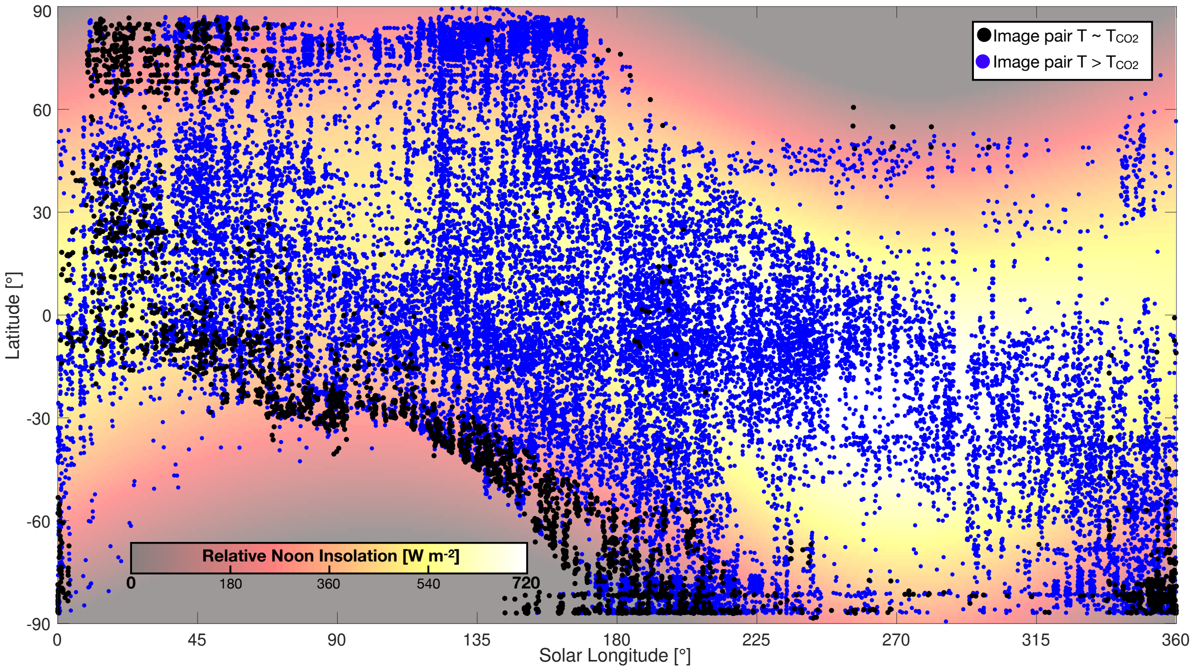

Figure 2. Spatial and seasonal distribution of THEMIS visible/thermal infrared pairs acquired when the sun incidence angle was between 70° and 110°. The colored background indicates the seasonality of direct solar illumination (top of the atmosphere) as calculated by a Keplerian orbital model used by KRC (Kieffer, 2013). An evident data distribution bias caused by operational, local weather, and illumination constraints exist across the dataset. As a result, surface coverage in the northern high/mid latitudes is more sparse than at other seasons/locations.

vations that are acquired during the afternoon are not used because not associated with diurnal CO_2 ice. This selection criterion yields a hemispheric bias (Fig. 2), as far fewer visible wavelength images at dawn meeting these criteria were acquired in the Northern hemisphere compared to the Southern hemisphere. Nonetheless, global sampling at all seasons is available and adequate for this work.

Surface temperatures are derived from THEMIS band 9 centered at 12.57 μm as they offer the best signal on cold surfaces (noise equivalent delta temperature of 1 K at 180 K (Christensen et al., 2004), estimated to 3 K at 150 K (Pilorget et al., 2013)), and because they have frequently been used for polar studies (e.g., (Kieffer et al., 2006; Pilorget et al., 2013; Piqueux & Christensen, 2008; Piqueux et al., 2008)). We eliminate image pairs clearly impacted by calibration issues (e.g.,(Edwards et al., 2011)), poor observation conditions (mainly the identifiable presence of clouds in visible wavelength imagery), or defined in the infrared by the coldest scene on the image smaller than 0.9 times the local CO_2 frost point T_{CO_2} calculated as follow:

$$T_{CO_2} = \frac{\beta}{\gamma - \ln(P)} \tag{2}$$

with $\gamma = 23.3494$ [1], $\beta = 3182.48$ [K] (James et al., 1992), and P, the local CO_2 partial pressure taken as 0.96 (Mahaffy et al., 2013) of the total surface pressure derived from the local topography and parametrized surface pressure observations (Withers, 2012). This selection criterion stems from the fact that on Mars, atmospheric CO_2 is in quasi-unlimited supply for overnight condensation at the surface and therefore any surface at

T_{CO_2} must be associated with the presence of carbon dioxide ice. Such selection is based on the assumption that no surface can be colder than the kinetic temperature of CO_2, and CO_2 ice of large grains has a high emissivity near 12.57 μm (Hayne et al., 2012). However, deposits composed of ice crystals with size of nearly 1 μm should lead to low emissivity surfaces, even at 12.57 μm (Piqueux et al., 2016), and could thus induce $T_{surf} < 0.9 \times T_{CO_2}$. Nevertheless, observations in the polar regions have demonstrated that such occurrences are rare (Forget et al., 1995; Forget & Pollack, 1996; Forget et al., 1998; Colaprete & Toon, 2002; Hayne et al., 2012, 2014) and generally associated with the presence of snow falls that are not expected near the equator.

To account for the instrument noise and possible atmospheric contributions that may approach a few K when looking at cold surfaces, we assign a 5 K tolerance for the identification of surface CO_2 ice. In other words, CO_2 is considered present on any surface where the local temperature is within 5 K of the predicted frost point based on the local atmospheric pressure and Eq. (2). This is a conservative approach based on work by Pilorget et al. (2013), who found that a 7 K margin is reasonable to identify CO_2 ice. Out of the 32,236 THEMIS images pairs inspected, 3,258 (i.e., $\sim$ 10%) are associated with temperatures requiring the presence of CO_2 ice on the ground.

Once an image pair is flagged for CO_2 ice based on the surface temperature, we inspect the associated visible wavelength image to identify surface frost patches. This characterization is performed using the THEMIS public viewer at `viewer.mars.asu.edu/viewer/themis`, with colorized THEMIS visible wavelength images, as surface frost seems to be indiscernible in greyscale images alone at high solar incidence angles, without further processing. The THEMIS visible camera has a resolution of 18 m/pixel and has five filters with band centers located at 425 (band 1), 540 (band 2), 654 (band 3), 749 (band 4), and 860 nm (band 5) (Christensen et al., 2004). When available, we used "R2B" images, a colorized product where of band 4 (red) and band 1 (blue) are combined using $0.65\times$ band 1 + $0.35 \times$ band 4 to generate a simulated green band used for the RGB composite (Bennett et al., 2018; Murray et al., 2016). When not available, we used conventional RGB composite resulting from band 4 (or, if not available, band 3), band 2, and band 1 in the blue channel (Bennett et al., 2018; Murray et al., 2016). Surface frosts are identified based on their blue/white hues, in stark contrast with the orange/brown/grey surrounding terrains, in spite of the challenging illumination conditions (Fig. 3). The vast majority of these blue/white units are confidently attributed to the surface (as opposed to the atmosphere) based on their sharp boundaries following morphometric or color units, topography, or preferential slope orientation. Some image pairs with blue/white patches are disqualified because they show evident calibration issues most likely due to the challenging illuminations conditions encountered at the terminator, where THEMIS was not originally designed to operate. Such images show unrealistic large bright color patches often associated with ghosts or individual wavelets, and/or no surface pattern. Another subset of images displays blue/white signatures with blurry boundaries, possibly indicating that hazes or clouds might be present and are not further considered for this work. Among the 3,258 image pairs associated with temperatures consistent with CO_2 ice, 2,761 images (i.e., $\sim$ 85%) show no calibration issue and contain potential surface frost signatures in visible wavelength. A confidence level for surface frost identification upon visual inspection is defined by assigning each image to one of five classes defined as follows:

- Class 1 (Fig. 3a, 115 images that account for 6% of visible wavelength detections): Excellent contrast between blue/white surface patches and nearby units characterized by very different colors (generally orange, brown, grey), adequate illumination conditions, geomorphological surface features (i.e., craters, scarps, plains, hills, etc.) perfectly recognizable. In this class, images display no perceivable calibration artifacts, and the spatial distribution of these blue/white surface patches

generally shows some spatial coherence, favoring pole facing slopes and flat surfaces. Class 1 image pairs are mainly located between 50°S and 30°S (Fig. S1);
- Class 2 (Fig. 3b, 534 images that represent 28% of the visible wavelength detections): Good color contrast between the blue/white surface units and the rest of the scene, and illumination conditions adequate for geological mapping but not ideal, resulting in harder-to-detect blue/white units, but still perfectly distinguishable. Slope patches are generally still fairly easily identified, but blue/white units on flat surfaces are more challenging. Some images display ghosts or under-saturation that sometimes results in an artificial enhancement of purple hues, decorrelated from surface morphology. Class 2 image pairs are preferentially found at mid and tropical latitudes (Fig. S1);
- Class 3 (Fig. 3c, 708 images that represent 37% of the visible wavelength detections): Fair contrast between blue or white surface units and the surrounding background, patches difficult to detect. However, high coherence with specific slopes and slope azimuth provides higher frost identification confidence. Image pairs in this class are either 1) of high intrinsic quality (contrast, saturation), but the blue/white units do not particularly stand out relative to the surrounding terrains as in Class 1 and 2, or 2) difficult to identify because of low contrast, obvious color artifacts, ghosts, and also because of the potential presence of near-surface hazes. Class 3 images have been detected at mid and high latitudes (Fig. S1);
- Class 4 (Fig. 3d, 556 images that account for 29% of the visible wavelength detections): Poor contrast between discreet blue/white units and the nearby terrains, resulting in speculative identifications, sometimes because of overall low image quality due to the extremely challenging illumination conditions encountered at the terminator, sometimes because of the subtle color contrast with the regional terrains. In Class 4, the size, shape and sometimes distribution of white/blue patches within the images allow us to confidently exclude hazes, or color processing artifacts. Class 4 images are more generally found at mid latitudes, between 25° and 30°S or polar latitudes (Fig. S1);
- Class 5 (Fig. 3e, 848 images): No identification of blue or white surface suggestive of surface frost despite surface temperatures consistent with the presence of CO_2 ice.

This classification is designed with the underlying assumption that the blue/white patches observed invisible wavelength images are indeed due to surface ice given the presence of CO_2 ice-like surface temperatures. This assumption is reasonable given our experience with mid-afternoon THEMIS visible wavelength imagery: high afternoon surfaces temperatures inconsistent with the presence of frost do not display patches such as those presented in Fig. 3.

3 Results

The spatial distribution of surface units at the CO_2 frost point where visible wavelength imagery is also available and without indications of calibration issues near dawn is shown in Fig. 4. THEMIS surface temperatures acquired at sunrise are consistent with the presence of CO_2 frost at virtually all latitudes (black and white dots in Fig. 4), confirming results presented by others with MCS (Piqueux et al., 2016) and THEMIS (Khuller et al., 2021a) data. THEMIS images presenting surface temperature close to T_{CO_2} cluster at the seasonal polar caps, at high latitudes in the North (up to 60°N) and middle latitudes in the South (down to 20°S), and the dusty terrains with low thermal inertia of Tharsis, Elysium, and Arabia Terra. No thermal images show temperatures close to T_{CO_2} at low latitudes in areas with high thermal inertia because these units have surfaces that are too warm at night to allow CO_2 condensation. Fewer occurrences of CO_2 frost are reported in Fig. 4 compared to the mapping results in Khuller et al. (2021a) because these authors did not use a visible wavelength image presence requirement, which

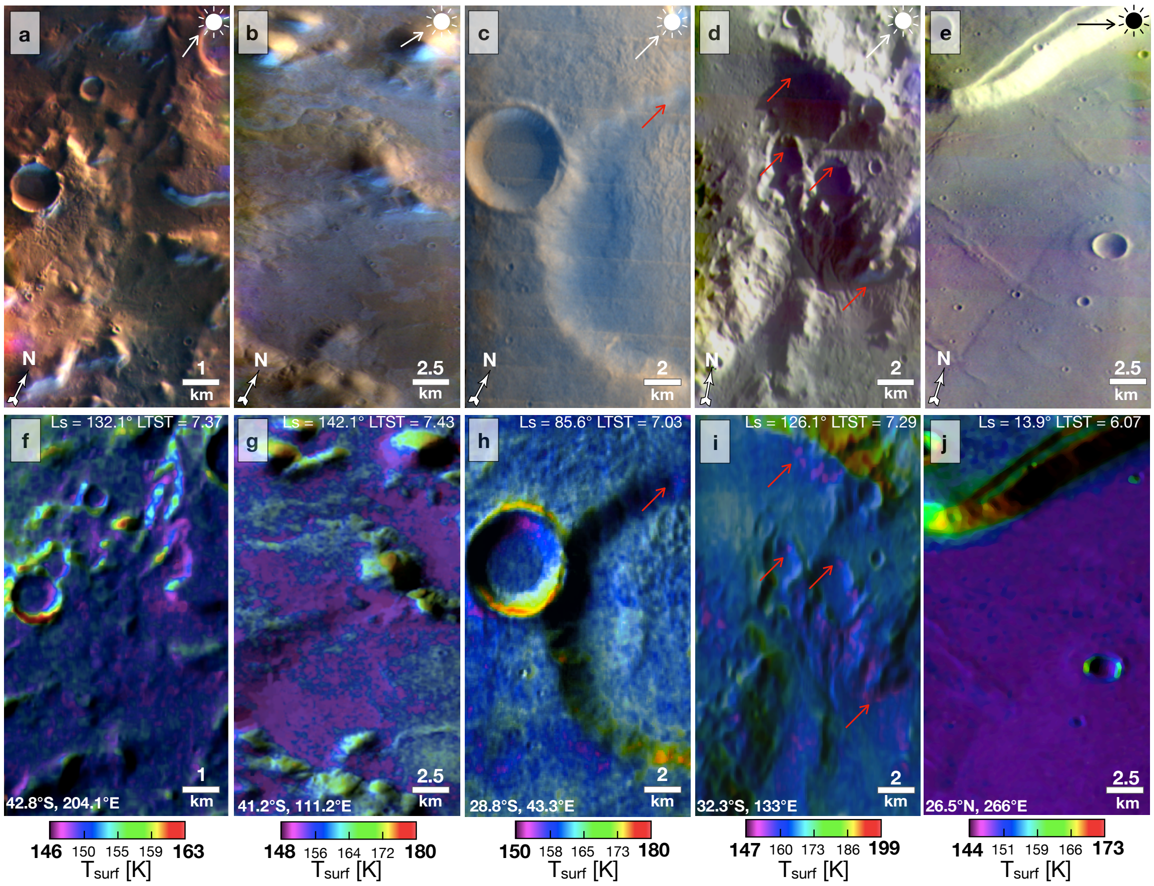

Figure 3. Examples of THEMIS visible wavelength (a-e) and corresponding thermal infrared (f-j) images acquired simultaneously near dawn. The blue/white surface patches (a-d) and low surface temperatures within 5 K of T_{CO_2} in infrared images (f-j) are interpreted as frost (Classes 1-4, see text for definition). Class 5 (no frost signature) despite surface temperatures consistent with CO_2 frost is illustrated with (e) and (j). Coordinates, solar longitude (Ls), and local true solar time (LTST) are given in the different panels. Red arrows emphasize hard-to-distinguish blue/white patches. White arrow point to the position of the sun in the sky. a: Class 1, V71796004; b: Class 2, V63705007; c: Class 3, V78900003; d: Class 4, V63305007; e: Class 5, V76958011; f: I71796003 associated with a; g: I63705006 associated with b; h: I78900002 associated with c; i: I63305006 associated with d. j: I76958010 associated with e (Christensen et al., 2002). f-j underlain with a THEMIS daytime IR mosaic to enhance topography (Edwards et al., 2011). Some terrains appear black in the thermal infrared images because of the background mosaic (not because of an absence of measurement).

drastically limits the number of usable infrared observations, and they applied a looser CO_2 ice temperature identification criterion (e.g., 7 K vs. 5 K tolerance on T_{CO_2}).

In the Southern hemisphere, blue/white patches at the CO_2 frost point are observed on visible wavelength imagery at latitudes as low as $\sim$ 20°S, noticeably closer to the equator than a previous analysis of bright patches in THEMIS visible wavelength imagery, e.g., 33°S (Schorghofer & Edgett, 2006), and $\sim$ 35°S based on Observatoire pour la Minéralogie, l'Eau, les Glaces et l'Activité (OMEGA, Bibring et al. (2004)) spectral identifications (Vincendon et al., 2010). This difference confirms the high sensitivity of our surface frost identification approach. A strong dichotomy appears between the North and the South, resulting from several factors. First, the southern winter lasts longer, favoring the accumulation of more ice at lower latitudes. Second, far fewer images have been acquired in the North than the South during the winter, for operational reasons. Third, the southern hemisphere is much older and therefore rougher than the northern hemisphere (Aharonson et al., 2001; Kreslavsky & Head, 1999; Kreslavsky & Head, 2000), with significantly more occurrences of pole facing terrains there where seasonal ice can survive longer, thanks to reduced direct insolation. Finally, the clarity of the atmosphere tends to be higher through the Southern polar vortex compared to the Northern one. In the North, the seasonal coverage after Ls $\sim 270°$ is too sparse to precisely determine the spatiotemporal envelope for frost presence. Nonetheless, frost occurrences are identified over a wide range of latitudes.

Despite more restrictive ice detection criteria than used in previous studies (Piqueux et al., 2016; Khuller et al., 2021a), our approach shows a similar or higher sensitivity at visible wavelengths given the lower latitudes of frost identifications. Yet, we still find 848 image pairs (out of 2,761, i.e., $\sim 30\%$) that do not show a signature of frost in visible wavelength imagery, while the ground is at CO_2 ice temperature. Noticeably, no identification in visible wavelength imagery is located in the 45°N-15°S latitude band in the low thermal inertia terrains (i.e., purple in Fig. 4, defined as thermal inertia < 100 J m^{-2} K^{-1} s$^{-1/2}$), where widespread diurnal CO_2 frost forms during a significant fraction of the year (Piqueux et al., 2016). In contrast, at other latitudes, 87.5% of the image pairs at the CO_2 frost point temperature are associated with bright patches on the ground (whether contaminated by water ice or not). This difference in morning frost identifications at visible wavelength suggests a distinct optical behavior of diurnal CO_2 frost when it is associated with dusty low thermal inertia terrains compared to CO_2 frost elsewhere on the planet, whether it is diurnal or seasonal, contaminated by water ice, sedimented dust, or either. This absence of identifications in visible wavelength imagery on dusty CO_2 cold surfaces could potentially be biased by observational factors, including:

- Poor contrast between the bright Martian dust and surface frost, resulting in seemingly no frost signature on dusty regions. The Martian dust is associated with the highest visible and near-infrared lambertian albedo units (excluding polar ice-exposing terrains), i.e., 0.27 (Putzig et al., 2005). This configuration is unlikely because the identification criterion for frost in visible wavelength images is based on the presence of blue/white hues, and as such, frosts seem perfectly distinguishable from regular darker colored warm surfaces (Fig. 3). In addition, we have identified blue/white surface units in high thermal inertia/albedo/dust cover index areas (Ruff & Christensen, 2002), near 180-270°E and 20-30°S (Fig. 4), further confirming that our mapping approach has a demonstrated capability to identify surface frost using visible wavelength imagery on high albedo, bright dust-like terrains. For these reasons, an absence of contrast or color between frost and the Martian dust does not seem to explain the systematic absence of frosted surfaces in visible wavelength imagery on low thermal inertia terrains. In brief, we acknowledge that a regolith/ice relationship diagnosis solely based on terrain color can be complicated by the lowering of the ice's albedo by dust (e.g., Khuller et al. (2021b) with water ice, Singh and Flanner (2016)). To mitigate this potential limit, we have derived the emissivity of these frosted surfaces at 12.57 μm as emissivity is diagnostic of ice presence (see section 2.1). A future study could contribute to this regolith and ice characterization by performing a thorough analysis of the spectral properties of these terrains using more THEMIS bands.
- Clean frost layers growing on the top of the regolith are optically thin at visible wavelengths, thus indistinguishable in visible wavelength imagery because too thin, similar to a model proposed by Svitek and Murray (1990) for water ice frost at the Viking 2 landing site. While it is certainly possible that an unknown fraction of the image pairs we flagged may be concerned with optically thin layers of frost,

> we eliminate a systematic bias because 1) the equivalent thickness of diurnal CO_2 frost frequently approaches several tens to hundreds of microns at dawn in the low thermal inertia regions (Piqueux et al., 2016), and 2) we have discussed in section 2.1 of this paper how such frost layers should be associated with pronounced albedo signatures.

For these reasons, we conclude that diurnal CO_2 ice should generally be distinguishable at visible wavelengths, and therefore the absence of identification implies very low contrast compared to unfrosted terrains. Quantitatively, the frequency of positive correlation between T_{CO_2} (Eq. (2)) and blue/white surfaces is insignificant for low thermal inertia terrains where diurnal frost is present (i.e., 5.5% of the images where the thermal inertia < 100 J m^{-2} K^{-1} s$^{-1/2}$ are associated with blue/white bright surfaces), but high with medium/high thermal inertia terrains (78.5% of the images where the thermal inertia > 100 J m^{-2} K^{-1} s$^{-1/2}$ are associated with blue/white bright surfaces, Fig. 5a). The 5.5% blue/white surface images pairs on low thermal inertia terrains are grouped near 15°S and 200-225°E, and are associated with unique intrinsically blue/white-colored surfaces (see for instance images V71284003/I71284002; V67886003/I67886002 (Christensen et al., 2002)). These occurrences seem thus to have no relationship to surface frost but we have reported them in Fig. 4 for completeness (Class 2). If ignored, our survey shows that no image associated with blue/white bright surfaces are found on low thermal inertia < 100 J m^{-2} K^{-1} s$^{-1/2}$ terrains.

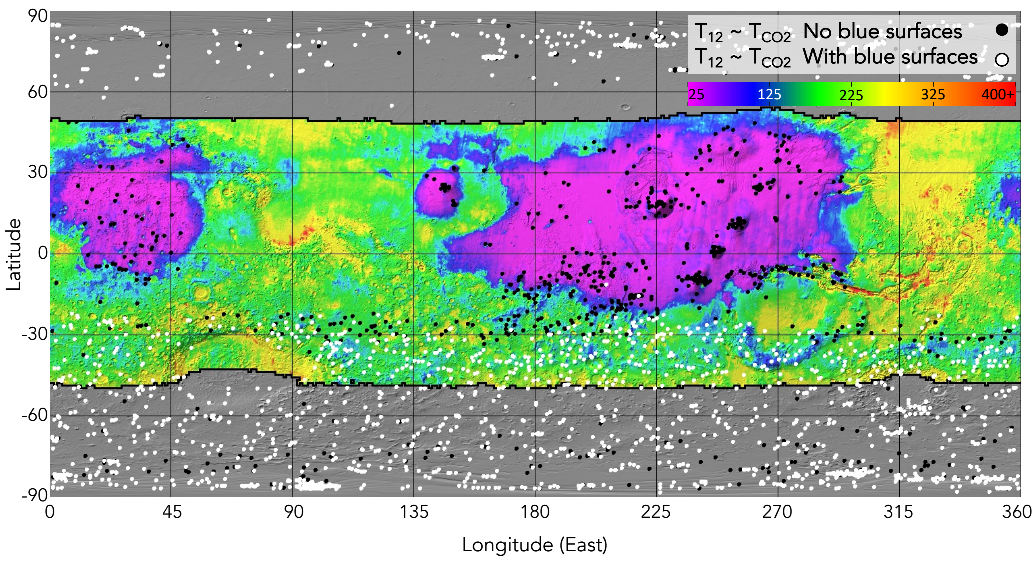

Figure 4. Distribution of dawn THEMIS visible and infrared wavelength image pairs within 5 K of the local CO_2 frost point (see text for the list of image pair selection criteria) corresponding to classes 1-4 (see Fig. 3). Black dots indicate no signature of frost in visible wavelength images (848 images, Class 5). White dots indicate the presence of image pairs where frost is identified at visible wavelengths (1,931 cases). Colorized background is a thermal inertia map (scale bar in J m^{-2} K^{-1} s$^{-1/2}$), from Christensen et al. (2001) overlaid on with a MOLA shaded relief (Zuber et al., 1992), only shown outside the maximum extent of the continuous seasonal caps (Piqueux et al., 2015). During the winter, the Northern high/mid latitudes are subject to much fewer observations than the Southern high/mid latitudes, partially explaining the hemispheric asymmetry (see Fig. 2 and associated text).

In other words, when the thermal inertia < 100 J m^{-2} K^{-1} s$^{-1/2}$, i.e., when the surface grain size $R < 20$ μm in diameter (Presley & Christensen, 1997), visible wavelength images do not display a diurnal frost signature. In contrast, the ratio of images presenting a signature at visible wavelengths over the total number of images in our dataset approaches 70-80% for $R > 20$ μm (i.e., most of the typical Martian regolith (Kieffer, 2013)). Most of the missing frost signatures in visible wavelength imagery when the surface temperatures at T_{CO_2} at high latitudes are generally linked to poor image quality, with challenging illumination conditions that prevent us from clearly assessing the color of the surface. This difference suggests that on low thermal inertia terrains, the visible wavelength optical properties of diurnal frost are uniquely dominated by those of the surface dust.

For completeness, we mention here that our mapping approach presents two important limits: 1) the impact of H_2O ice on frost signatures at visible wavelengths is not considered, and 2) there is no formal distinction between seasonal versus diurnal ices.

- 1: Some water ice may be cold-trapped on CO_2-cold surfaces, but we are unable to characterize its effect in terms of visible wavelength imagery signature. Indeed, previous work has shown that seasonal water ice deposits may be important contributors to surface blue/white hues in visible wavelength imagery (see for instance Bapst et al. (2015)), if not too contaminated by dust ($<$ 1% dust contamination, Khuller et al., 2021b). Similarly, Kieffer (1968) showed that small amounts of water frost can mask CO_2 frosts. However diurnal deposits may not have adequate time to form thick-enough deposits to be visible on the ground (Martínez et al., 2016). Therefore, it is questionable whether an absence of diurnal frost signature in visible wavelength imagery on low thermal inertia terrains is biased by the effective absence of water ice cold-trapped with CO_2 ice. A differential signature between seasonal and diurnal CO_2 frost due to water ice veneers is not fully supported by OMEGA observations of low latitude seasonal CO_2 ice not obscured by water ice veneers (Vincendon et al., 2010);
- 2: The lack of overlapping visible wavelength observations at different local times prevents us from determining whether blue/white units are sometimes, if ever, associated with diurnal CO_2 ice. In other words, the blue/white occurrences might all be associated with seasonal CO_2 ice, and diurnal CO_2 ice does not form blue/white patches, regardless of regolith grain size and properties. Nevertheless, CO_2 ice detected in thermal infrared data at low latitudes in the low thermal inertia regions (purple units in Fig. 4) must be diurnal because these terrains are much too warm for CO_2 ice survival during the day (Piqueux et al., 2016), at any conceivable spatial scale and season. Therefore, our approach is indeed able to single out a large body of diurnal CO_2 frost occurrences between 45°N and 15°S.

The emissivity of frosted terrains in the low thermal inertia regions can also constrain the nature of the CO_2 ice/regolith relationship. As mentioned in section 2.1, ice deposits with micrometric grain size are expected to decrease the emissivity of the surface, especially in THEMIS band 9 data used here. As a result, brightness temperatures are expected to be lower than T_{CO_2} (Piqueux et al., 2016). For each THEMIS image (even those with $T < 0.9 \times T_{CO_2}$) acquired over the low thermal inertia terrain, we extract the averaged surface temperature T_{surf} to derive the surface emissivity ϵ (Fig. 5b) with:

$$\epsilon = \frac{T_{surf}^4}{T_{CO_2}^4} \tag{3}$$

Figure 5b shows that most of THEMIS images in dusty grounds display a high surface emissivity, close to the emissivity of ice-free dusty grounds (0.96, (Ruff & Christensen, 2002; Piqueux et al., 2016)). After removing problematic (i.e. calibration issue) images,

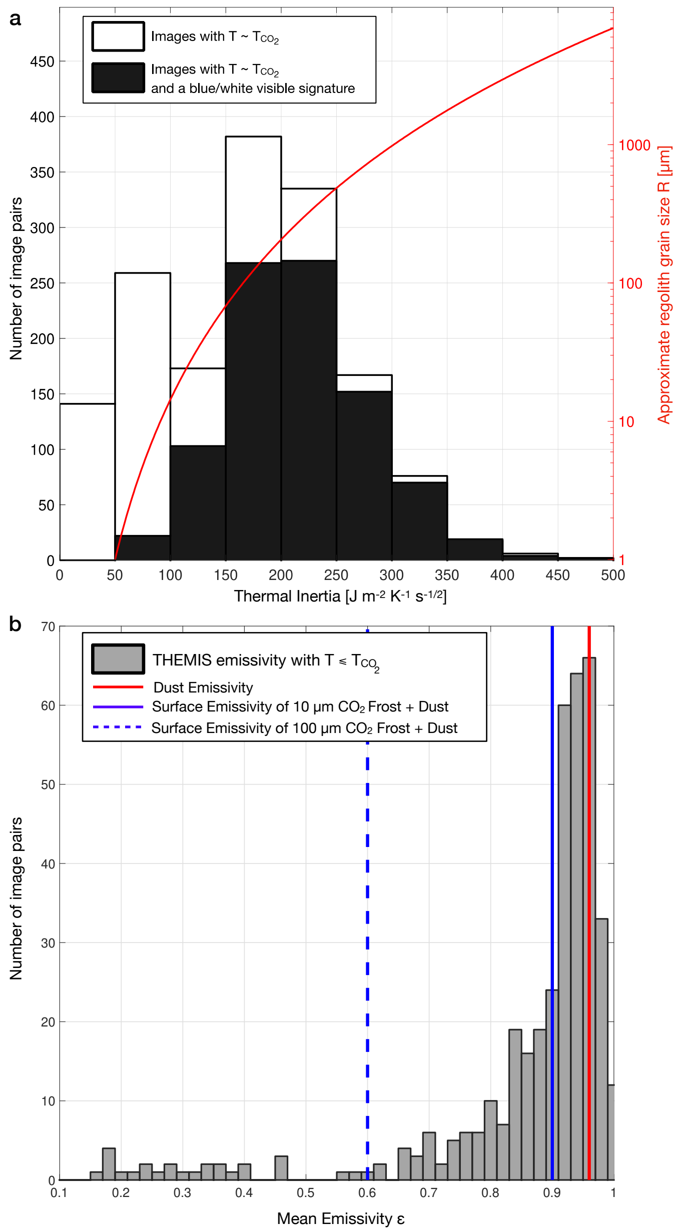

Figure 5. Thermal inertia values of the terrains associated with images pairs at T_{CO_2} (Christensen et al., 2001). The approximate relationship between thermal inertia and grain size is indicated in red (Presley & Christensen, 1997; Kieffer, 2013). Images pairs at T_{CO_2} on low thermal inertia terrains (i.e., < 100 J m^{-2} K^{-1} s$^{-1/2}$, $R < 20$ μm) are rarely associated with a frost signature at visible wavelengths, and most are located at high latitudes, see Fig. 4). b: CO_2 emissivity derived at $\lambda = 12.57$ μm. Dust emissivity at 12.57 μm (red line) from Ruff and Christensen (2002). Modeled emissivity of the dusty surface overlaid by 10 μm (solid line) and 100 μm (dashed line) CO_2 ice layer indicated in blue (Piqueux et al., 2016).

we find that more than 70% of the images show a CO_2 frosted surface emissivity between 0.96 $\pm$ 0.04 (uncertainty defined as the 3-σ spread from our 5 K tolerance, see section 2.2). Such high emissivities at 12.57 μm indicate the absence of CO_2 frost over dusty surfaces, or over micrometer size thickness (Fig. 11 in Piqueux et al. (2016)). But in the latter case the ice thicknesses would be inconsistent with mass/energy balance results (Piqueux et al., 2016). Thus, the high surface emissivity values are most consistent with an absence of frost on the surface.

The visible and thermal infrared observations could conceivably match other regolith/ice configurations and formation models than the one presented here (Fig. 1); however, this regolith/ice model is based on reasonable theoretical reasonings, and our work shows that the observations we present are consistent with this model. Pathological regolith/ice configurations or alternate ice growth models could match the observations, but they would require still-to-be-proposed formation models compared to what is presented here. The observations are consistent with dirty diurnal CO_2 ice in these terrains, following the hypothesis formulated by Piqueux et al. (2016) , and illustrated in Fig. 1.

4 Discussions

4.1 Destabilization of a dust grain trough CO_2 sublimation

The sublimation of seasonal carbon dioxide frost has been associated with numerous processes shaping the surface of Mars (Dundas et al., 2012; Dundas, 2020; Diniega et al., 2013, 2021; Hansen et al., 2013; Pilorget & Forget, 2015; Piqueux et al., 2003, 2008). Similarly, we propose to quantitatively describe the interaction between the sublimating diurnal CO_2 frost and the surface layer.

Based on theoretical models, laboratory experiments, and field observations on Earth (with water frost), we hypothesize that the recurring growth and removal of ice may create a stress cycle in the regolith leading to internal grain displacement and microscopic weathering (Everett, 1961; Ruedrich & Siegesmund, 2006; Woronko & Pisarska-Jamroży, 2015). On Mars, at sunrise, the rapid sublimation of the diurnal ice creates a short-lived wind field within the regolith that exerts a drag on individual grains, opposite in direction to gravity and cohesion forces, somewhat similar to models proposed for the sublimation of translucent seasonal CO_2 ice sand grains at high latitudes (Kieffer et al., 2006; Kieffer, 2007; Pilorget & Forget, 2015). However, we reiterate that this model is unique to the low latitudes of Mars where low thermal inertia terrains conducive to the formation of diurnal ice exist. This restriction stems from the need of regolith grains smaller in size than the typical path length of photons emitted at the peak emission wavelength (Fig. 1). These conditions are met in the lowest thermal inertia terrains, not found in the polar regions of Mars.

We note that the upward movement of dust grains in relation to CO_2 ice sublimation is a distinct process from saltation, a process well known to occur on Mars with sand-size grains (Greeley, 2002; Greeley et al., 1976; Greeley et al., 1980, 1992; Merrison et al., 2007). A lift force is always orthogonal to the flow that creates it, by definition, and is the root cause of the saltation process. Saltation models consider grains subjected to forces induced by horizontal winds. With saltation, gas flow around grains is not symmetrical, inducing a circulation that causes the lift following the Kutta-Joukowski theorem (Sears, 1981). Motion starts with a rotational component.

In contrast, the grain levitation model we propose differs from saltation models (Fig. 7a) in that the movement caused by the drag is parallel to flow lines, not orthogonal. In contrast to the saltation model, the flow of CO_2 gas around the grain is symmetrical, without circulation and therefore without the lifting described in saltation models by the Kutta-Joukowski theorem. The drag caused by the gas itself on the grain sets the dust grains in motion. When the normal component of the drag is larger than the combination of the normal component of the gravity and cohesion forces, grain movement occurs without any rotation. To avoid confusion, in this paper, we describe the movement of grains as "upward movement" as opposed to "lift" because lift implies orthogonality between gas flow and grain movement (saltation). This model considers that CO_2 sublimation only acts one single dust grain at a time, and ignores diffusion trough the granular medium.

The drag F_d on individual grains created by the moving CO_2 gas is proportional to the gas flow velocity $w(t)$ [m s^{-1}]:

$$F_d = \frac{1}{2}\rho w^2 S C_d \tag{4}$$

with $S = \pi R^2$ [m^2] the section of a spherical grain, C_d a dimensionless drag coefficient, ρ the density of CO_2 gas (0.02 kg m^{-3} (Owen et al., 1977)), R [m] the radius of dust particle in dusty low thermal inertia regions ($\sim$ 1 μm). The gas flow velocity $w(t)$ is primarily controlled by the solar energy input and CO_2 ice mass balance at the surface. To evaluate $w(t)$, we first calculate the frost thickness, following the approach presented by Piqueux et al. (2016). In short, when the surface temperature reaches T_{CO_2}, heat lost at the surface through radiation to the atmosphere (minus the downwelling radiance) is converted into a mass using the latent heat of condensation of CO_2. When the sun rises, heat is added to the system at the surface and leads to sublimation, creating a latent heat flux $LE(t)$. Quantitatively, the CO_2 ice thickness δ [m], and thus the frost mass, can be expressed as a function of the energy balance at the surface:

$$\rho_{i,c} L_e \frac{\mathrm{d}\delta^3}{\mathrm{d}t} = \epsilon\sigma T^4_{CO_2} - Q_{IR}(t) - (1-A) \times S_M(t) \times \cos(i(t)) \tag{5}$$

with $\rho_{i,c}$ the CO_2 ice density set to 1.6×10^3 kg m^{-3} (Mangan et al., 2017; Putzig et al., 2005), and L_e the latent heat of sublimation of CO_2 ice (5.9 10^5 J kg^{-1} (Pilorget & Forget, 2015)), ϵ the ice emissivity taken as 0.99 to be consistent with previous work from Piqueux et al. (2016), σ the Stefan Boltzmann constant, Q_{IR} [W m^{-2}] the atmospheric downwelling flux, A the lambertian vis/ near-infrared albedo of dusty surface set to 0.27 (Putzig et al., 2005), S_M [W m^{-2}] the insolation of the surface after atmospheric correction, and i [rad] the solar incidence angle. Q_{IR} and S_M are calculated using the numerical thermal model KRC (Kieffer, 2013). In our model (Fig. 1), the CO_2 ice crystals form at depth, within the first few microns to hundreds of microns under the surface, that is, at a depth three orders of magnitude smaller than the diurnal thermal skin depth in these terrains (i.e., 1-3 cm, (Grott et al., 2007)). Therefore, at dawn, the heat wave induced by direct solar insolation has to travel through a negligible distance compared to a diurnal skin depth to reaches the ice, in a matter of just a few tens or seconds to a minute. This time constant is ignored in our model.

The latent heat LE [W m^{-2}] released at the surface can thus be expressed as:

$$LE(t) = L_e \mid \frac{\mathrm{d}m_{ice}}{\mathrm{d}t} \mid = \mid \rho_{i,c} L_e \frac{\mathrm{d}\delta^3}{\mathrm{d}t} \mid = \mid \epsilon\sigma T^4_{CO_2} - Q_{IR}(t) - (1-A) \times S_M(t) \times \cos(i(t)) \mid \tag{6}$$

Latent heat is only released when $\delta(t) > 0$, i.e., when frost is still present at the surface. Therefore, Eq. (5) can be numerically integrated to derive $\delta(t)$. $LE(t)$ can then be computed from Eq. (6) when $\delta(t) > 0$.

The CO_2 gas created by this sublimation is generated uniformly in the pore resulting in a mass flow rate q [kg m^{-2} s^{-1}] perpendicular to the surface,which gives a mean gas velocity using Eq. (7) (Kieffer et al., 2000; Diniega et al., 2013):

$$w(t) = \frac{q}{\rho} = \frac{LE(t)}{\rho L_e} \tag{7}$$

To bound $w(t)$ in low thermal inertia regions, we use the season-dependent CO_2 frost thickness at dawn provided by Piqueux et al. (2016). Using Eq. (7), we compute the wind-driven velocity at a spatial resolution of one point per degree, 36 times per year to conform with the frost thickness maps of Piqueux et al. (2016). Frost thicknesses calculated by Piqueux et al. (2016) represent lower bounds because they assumed 0 frost thickness at 3 AM, when MCS observed the surface. They acknowledge that CO_2 frost may have formed earlier in the night, resulting in non-0 thicknesses at 3 AM. This assumption results in conservative wind speeds here, as more frost might be available for sublimation. Figure 6 shows the frequency distribution of peak wind velocity for each location on Mars where diurnal frost is expected to form. Values range from 2.3 mm s^{-1} to 3.2 cm s^{-1}, with 1.7 cm s^{-1} on average and a standard deviation of 0.8 cm s^{-1}, with the highest velocities associated with the thickest frost deposits and the lowest ground thermal inertia values. This range of gas velocities is generally consistent (although higher) than values reported by others for syn-regolith CO_2 winds, based on laboratory measurements (Sylvest et al., 2018) and numerical models both for seasonal ice sublimation (Kieffer, 2007) and Knudsen pumping (de Beule et al., 2013; Schmidt et al., 2017). The model presented here assumes uniform laminar flow, but turbulent eddies could conceivably be present and necessitate an additional diffusivity coefficient term in Eq. (7) (Brutsaert, 1982), resulting in lower wind values, and therefore fewer occurrences of regolith grains destabilization. Energy losses related to turbulent transport or the absorption of solar energy by the medium, reducing the energy brought to the ice crystals, are also neglected, which can lead to an overestimation of w. A full model of the drag on grains would require a significantly more complex mathematical treatment (see for instance Hu (2019)), beyond the scope of this paper. The approach presented here solely aims at evaluating whether diurnal frost sublimation can conceivably destabilize sloped terrains.

The resulting drag can then be calculated assuming an incompressible laminar flow. The Reynolds number is given by:

$$Re = \frac{\rho w 2R}{\mu} \tag{8}$$

where $\mu = 7.42 \times 10^{-6}$ [Pa s] is the dynamic viscosity of CO_2 gas at 148 K given by Sutherland's law (Sutherland, 1893). With $w \leq 0.03$ m s^{-1} (Fig. 6), Eq. (4) can be simplified following a formulation by Yang et al. (2015):

$$C_d = \frac{24}{Re} \tag{9}$$

Introducing Eq. (8) and Eq. (9) in Eq. (4) , and deriving S with R yield to the final form of :

$$F_d = 6\pi R \mu w \tag{10}$$

For grain movement to occur, F_d must be larger than the combination of gravity F_g and cohesion forces F_c. Hence, vertical movement is possible when Eq. (11) is verified:

$$F_d \geq 2F_c \cos(\psi) + F_g \tag{11}$$

with ψ an angle describing the packing of grains (see Fig. 7a). The cohesive force between two spherical dust particles of radius R [m] can be expressed following an expression given by (Hartzell et al., 2013; Perko et al., 2001; Scheeres et al., 2010)

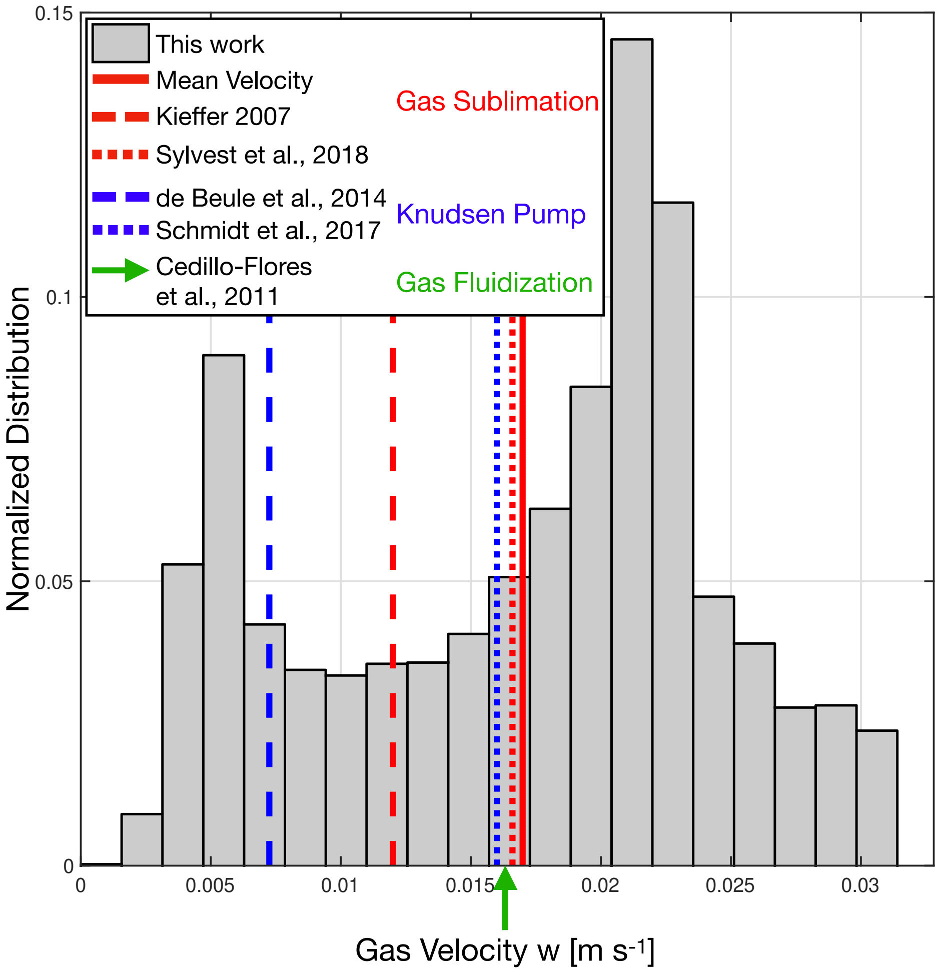

Figure 6. Distribution of the sublimation-driven wind velocities in the Martian regolith, and comparison with other published values (red) and those reported for Knudsen pump (blue). Each bin has been normalized by the total number of samples (2552884) to get a normalized distribution. The green arrow indicates the fluidization threshold beyond which avalanching becomes possible (Cedillo-Flores et al., 2011)

$$F_c = \alpha R \tag{12}$$

where α [N m^{-1}] is a cohesive parameter that depends on the physical and chemical properties of individual dust grains. Wind tunnel experiments with frost-free dust aggregates suggest that $\alpha \sim 10^{-5}$ N m^{-1} (Merrison et al., 2007). However, the presence of the frost (carbon dioxide and possibly water frosts) within the pores certainly increases the cohesion between grains (Greenberg et al., 1995; Perko et al., 2002). Consequently, it certainly impacts α. Furthermore, ice crystals might interact with electrostatic (Merrison et al., 2007; Sullivan et al., 2008) and/or magnetic (Kinch et al., 2006; Goetz et al., 2008) forces that hold dust grains together (none of which modeled here), possibly creating agglomerate dust forms rather than spherical grains (Kinch et al., 2015). A contrario, under terrestrial conditions, experimental work has demonstrated that recurring ice crystal formation and growth in porous media can generate sufficient stress leading to microscale physical weathering on individual grain, internal grain displacement, and even the rupture of cemented materials (Everett, 1961; Ruedrich & Siegesmund, 2006; Woronko & Pisarska-Jamroży, 2015), confirming that the presence of ice can also be a factor of reduced cohesion.

We can now compare the drag, cohesion and gravity forces with each other. The normal component of the buoyancy-corrected gravity to a spherical dust grain (Phillips, 1980) is given by:

$$F_g = \frac{4}{3}\pi R^3(\rho_g - \rho)g\cos(\theta) \tag{13}$$

with ρ_g the density of the grains set to 2500 kg m^{-3}, g the gravity set to 3.71 m s^{-2}, θ [degrees] the slope of the surface. Introducing Eq. (10), (12) and (13) into (11) leads to the final condition for the levitation of the grain:

$$6\pi R\mu w \geq 2\alpha R\cos(\psi) + \frac{4}{3}\pi R^3(\rho_g - \rho)g\cos(\theta) \tag{14}$$

A regolith dust grain moves upward if the velocity of the sublimation-driven CO_2 gas flow w is larger than a velocity threshold w_* [m s^{-1}]:

$$w \geq w_* = \frac{2\alpha R\cos(\Psi) + \frac{4\pi R^3}{3}(\rho_g - \rho)g\cos(\theta)}{6\pi R\mu} \tag{15}$$

w_* is computed for slope angles θ ranging between 0 and 30°, which corresponds to slopes commonly observed on Mars (Kreslavsky & Head, 1999; Kreslavsky & Head, 2000). The grain packing angle ψ theoretically ranges from 0 to 60°. As the low thermal inertia units are associated with very porous media (Presley & Christensen, 1997) , ψ should be high and is set to 60° in the following.

The wind velocity threshold w_* necessary for grain movement is shown in Fig. 7b as a function of grain size, local slope and cohesive parameter α. w_* is typically smaller than 3.5 cm s^{-1} for the 1-2 μm grains expected in 100 J m^{-2} K^{-1} s$^{-1/2}$ thermal inertia terrains with typical cohesive parameter $\alpha \sim 5\ 10^{-5}$ N m^{-1}. Under favorable conditions (see Fig. 7b), $w_* < 1$ cm s^{-1}. Sublimation-driven wind velocities w can reach this range of values (Fig. 6 and 7b), indicating that vertical drags are comparable or larger in strength to gravity and cohesive forces combined, and might be able to move individual grains upward at the time of peak CO_2 sublimation. Further, Fig. 7b confirms that the local slope and grain cohesive parameter also play an important role: flat or shallow sloped terrains are associated by larger w_* compared to steep slopes and grains are easier to move on surfaces that are already close to the angle of repose (30-35° (Kleinhans et al., 2011; Atwood-Stone & McEwen, 2013)). In addition, the grain packing angle seems to display an even larger control over w_*: larger ψ, i.e., looser packing, strongly decreases w_* compared to more compact grain arrangements (e.g., w_* for a micrometer dust grain on a 30° sloped surfaces and $\alpha = 5\ 10^{-6}$ N m^{-1} can change from 3.1 cm s^{-1} for $\psi =$ 60° to 5.5 cm s^{-1} for $\psi = 30°$). The low thermal inertia values associated with the dusty terrains on Mars require very low-density regolith, high porosity, and therefore high ψ, thus favoring grain movement. Generally, grains ~ 20 μm or larger cannot be displaced by this drag mechanism (Fig. 7b), but 1-2 μm uncohesive grains located on sloped terrains can be associated with a regime where frost sublimation can initiate grain movement.

Similar conclusions regarding the ability of subliming CO2 ice to displace regolith grains were drawn by Kieffer et al. (2000); Kieffer (2007) and Kieffer et al. (2006) for seasonal CO_2 sublimation near the poles fracturing a pressurized CO_2 ice slab that could promote the suspension of 1-2 μm dust grains. Our modeling results are also somewhat

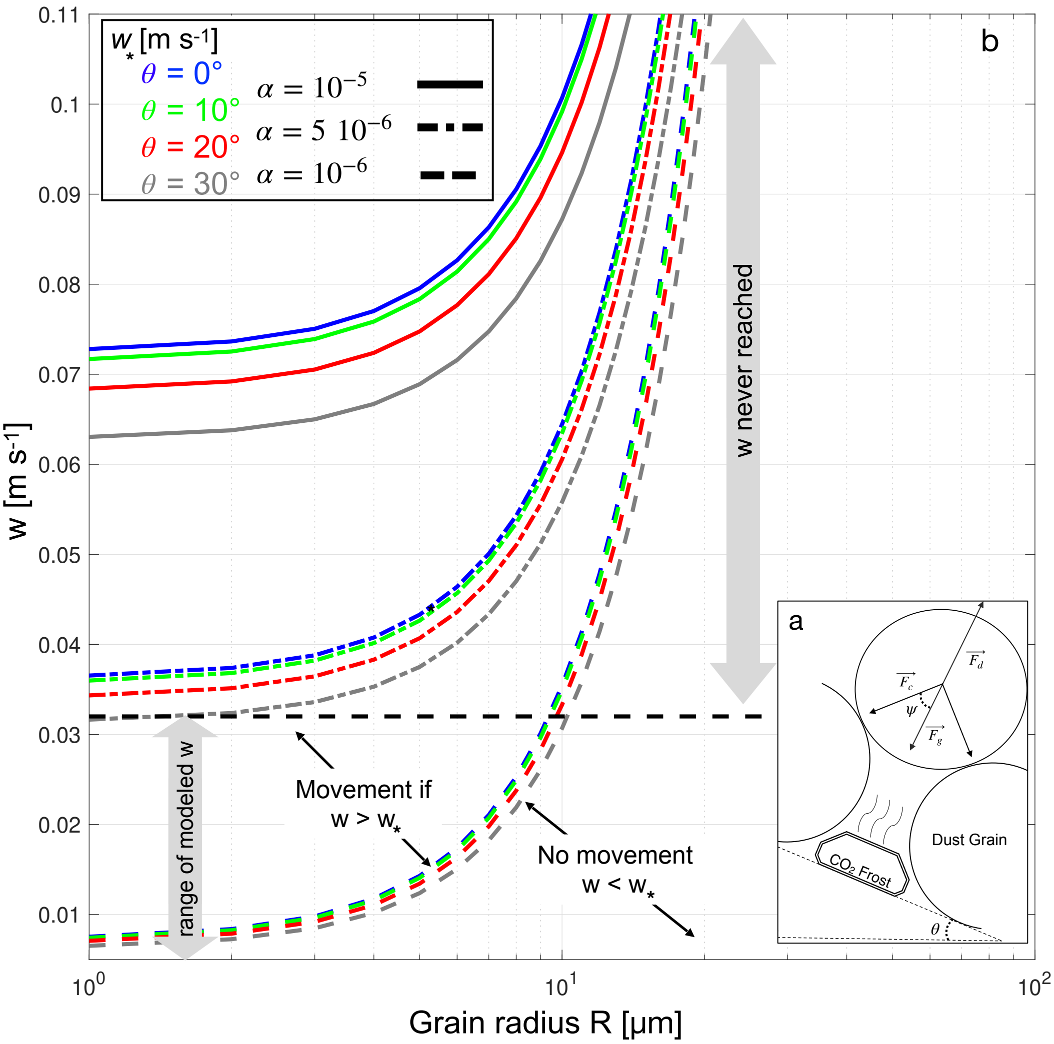

Figure 7. Regolith grain motion domains. a: schematic of the forces acting on a stationary regolith grain subjected to a drag caused by CO_2 frost sublimation. F_g is the gravitational force ; F_c an interparticle force; F_d is the drag. b: Velocity threshold w_* (colored lines) as a function of grain size, local slope θ, and cohesive parameter α for a packing angle $\psi = 60°$. Each curve delineates two domains: a domain "above" where grain movement is possible ($w > w_*$), and a domain "below", where grain movement is not possible ($w < w_*$). The horizontal dashed line marks the maximum modeled wind velocity (e.g., w = 3.2 cm s^{-1}, Fig. 6). Locally, dust grains can be moved upward if the wind velocity w is larger than the velocity threshold w_*. For the average wind velocity w = 2.3 mm s^{-1}, grains ~ 1-5 microns in size on steep slopes are in a domain where their movement is possible if the grains are not strongly bonded to each other ($\alpha \sim 10^{-6}$N m^{-1}, $w_* \sim$ 1mm s^{-1}).

comparable to laboratory observations of subliming CO_2 frost on sloped surfaces able to trigger downslope material movement (Sylvest et al., 2018), although significant experimental and modeling differences exist (i.e., the processes we describe here exclusively involves dust, whereas those experiments involved sand-size material; we assume near-sunrise illumination conditions whereas these experiments assumed mid-day insolation relevant to seasonal processes; and we assume extremely small amounts of ice compared to these experiments with CO_2 ice slabs). In addition, we occasionally derive large gas velocities $w > 0.0165$ m s^{-1} (Fig. 6) suggesting that fluidization of avalanching material becomes possible (Cedillo-Flores et al., 2011), indicating that under favorable conditions, dust grains put in movement along sloped terrains may therefore display a fluid-like behavior similar to that modeled by others (Miyamoto et al., 2004). We conclude that short-lived CO_2 sublimation-driven winds in the surficial regolith at sunrise can set individual surface dust grains in motion, preferentially on sloped, porous terrains composed of poorly cohesive dust grains, and can even lead to flow-like patterns.

Although this model indicates that the conditions are met to set individual dust grains in motion at the very surface of the regolith through morning CO_2 frost sublimation, vertical drag is expected to decrease shortly after the grains are displaced vertically. In other word, we do not suggest that this mechanism sends individual dust grains on ballistic trajectories above the ground, as proposed for the formation of fans and other features in the polar regions; but rather that grains rearrangement can occur, internal to the regolith in the top few 10's to 100's μm. During sublimation, the equivalent angle of repose is artificially and temporarily decreased, but material is not envisioned to depart from the surface.

4.2 The formation of Slope Streaks

Here, we hypothesize that this sublimation-driven slope destabilization can initiate and facilitate dust avalanching and the formation of slope streaks. Slope streaks (Fig. 8) are dark wedge-shaped surface features on sloped terrains, initiating at a point and broadening downslope (Chuang et al., 2007; Ferris et al., 2002; Kreslavsky & Head, 2009; Miyamoto et al., 2004; Phillips et al., 2007; Schorghofer et al., 2002; Sullivan et al., 2001). Work by (Chuang et al., 2007) also shows that slope streaks are associated with mass movement downslope, and are not limited to a simple darkening of the surface.

A survey by Bhardwaj et al. (2019) using the High Resolution Imaging Science Experiment (HiRISE, McEwen et al. (2007)) data shows that the length of slope streaks varies from 14 to 1600 m, and their widths range from 1 to 148 m. They exhibit a wide variety of morphologies, including linear, curved, and fan shaped (Bhardwaj et al., 2019). The vast majority of slope streaks is found on dusty low thermal inertia surfaces (Baratoux et al., 2006; Kreslavsky & Head, 2009), and work by Heyer et al. (2019) seems to highlight a loose relationship between formation rate and seasons, in contrast with a previous study that did not show any seasonality in the development of new streaks (Schorghofer & King, 2011).

The formation process for slope streaks is still debated, and generally falls into two categories: wet vs. dry mechanisms, although both types can be associated with dust avalanches. Wet processes involve episodic seeping of transient liquids generating low-albedo oxides that precipitate as slope streaks (Mushkin et al., 2010), subsurface water ice melting that triggers dust avalanches (Schorghofer et al., 2002), and regolith darkening through seasonal iron oxide precipitation associated with chloride brines resurgence originating from shallow ice reservoirs (Kreslavsky & Head, 2009). In this model, brines act as a lubricant facilitating the movement of dust particles. Dry mechanisms involve dust avalanches created by wind-regolith interaction (Baratoux et al., 2006; Chuang et al., 2007, 2010; Dundas, 2020; Sullivan et al., 2001), and surficial gravity-driven erosional processes followed by transport in the downslope direction (Phillips et al., 2007). In addition, some slope streaks seem to have been linked to specific triggering agents, including dust devils (Schorghofer et al., 2007), impact craters (Burleigh et al., 2012; Chuang et al., 2007), and rock falls (Chuang et al., 2007). However, the initiating and sustaining mechanism for the vast majority of observed slope streaks is not identified (Bhardwaj et al., 2019; Dundas, 2020), and Earth analogs have not been recognized. We propose a dry mechanism for the initiation and development of slope streaks involving the sub-

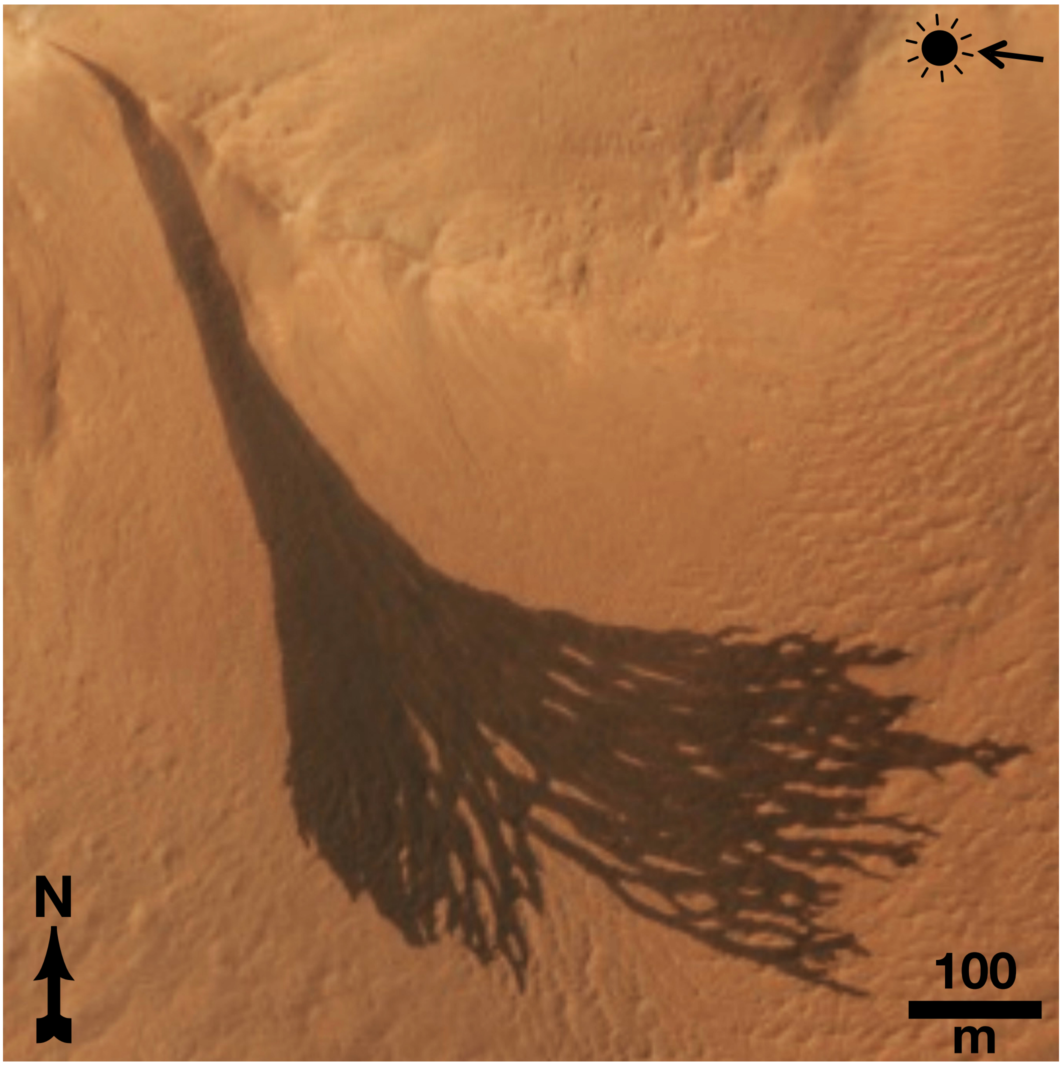

Figure 8. Example of a slope streak (HiRISE) ESP_053518_1955) on the Olympus Mons aureole (Lat = 15.23°N, Lon = 214.9°E, at Ls = 106.3°). The black arrow points the sun orientation.

limation of diurnal CO_2 ice on dusty terrains. In this model, diurnal CO_2 frost forms dirty ice within the top few tens to hundreds of microns of the dusty low thermal inertia regolith, where both diurnal frost and slope streaks are observed (Fig 9), but where no frost signature at visible wavelengths is recognized at dawn (Fig. 4). At sunrise, this diurnal frost sublimates, initiating a vertical drag on individual grains able to set those uncohesive in motion (Fig. 7). In this model, steep dusty terrains already close to the angle of repose (i.e., 30-35° (Kleinhans et al., 2011; Atwood-Stone & McEwen, 2013)) are destabilized and initiate an avalanche of dust. This model is consistent with the fact that typical slope associated with slope streaks is high, i.e., 25° (Brusnikin et al., 2016). Warmer subsurface dust gets entrained downslope and is placed in contact with the still-frosted pristine regolith surface. Sublimation is further promoted, fluidizing the material moving downslope.

This model requires slope streaks to initiate and develop in a relatively short period of time near dawn, when CO_2 frost is present and actively subliming. This predic-

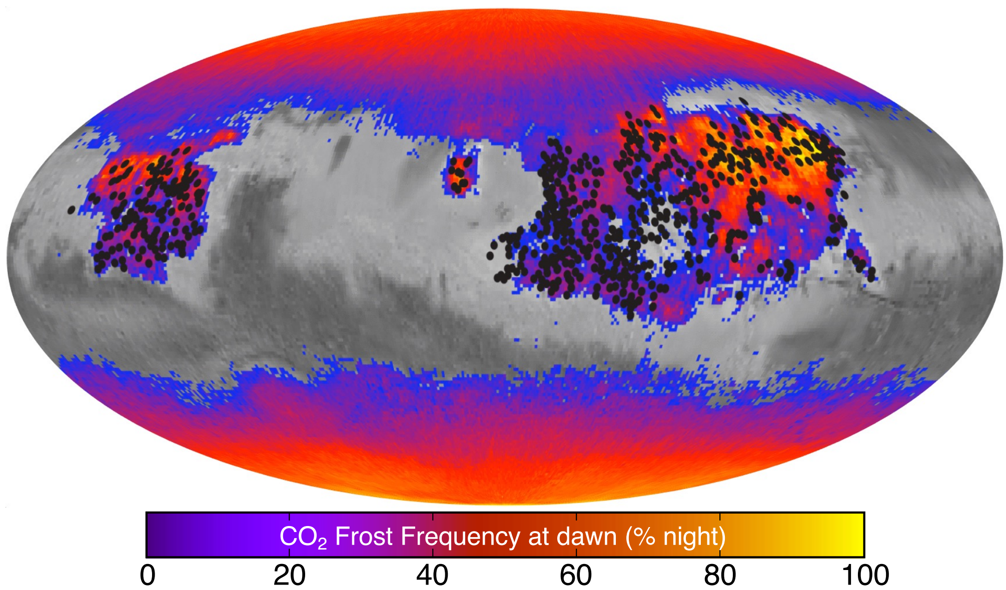

Figure 9. Distribution of slope streaks (black dots) extracted from (Schorghofer et al., 2007) and diurnal CO_2 frost distribution and frequency (adapted from (Piqueux et al., 2016)). No color is reported where no diurnal frost is modeled to be present at dawn. 0 means no diurnal frost ever, 100 means diurnal frost is present every dawn of the year. Background is a TES albedo map, Mollweide projection, 200°E prime meridian.

tion is consistent with observations by Aharonson et al. (2003) who noticed that slope streaks completely develop within a few sols at most, in contrast with Recurring Slope Lineae that develop over seasonal periods of time (McEwen et al., 2011). A triggering and sustaining agent associated with a relatively short dynamics disfavoring seasonal processes over diurnal (or shorter) processes is consistent with our proposed mechanism.

Our model also suggests that slope streaks should preferentially form on east or equator facing slopes, where CO_2 frost sublimation at sunrise is assumed to be most vigorous as they received more solar insolation. However, statistical work on slope streaks orientation does not confirm this prediction (Baratoux et al., 2006; Heyer et al., 2019; Schorghofer et al., 2002). Around Olympus Mons, slope streaks seem to form in a wide range of directions (Heyer et al., 2019), without a clear preferential east or equator facing orientation. This possible discrepancy between our model and the observations reported by Heyer et al. (2019) indicates that at a minimum, multiple factors control the initiation of slope streaks.

If triggered by subliming CO_2 ice, slope streaks might preferentially form near the top of sloped terrains where radiative coupling with adjacent surfaces is minimized (and therefore where CO_2 frost might preferentially form). Similarly, in our model, slope streaks should preferentially form overnight during the colder seasons. Slope streak formation seems to follow a mildly pronounced seasonality (Heyer et al., 2019; Schorghofer & King, 2011), but on the Olympus Mons Aureole, they form at all seasons, with a peak between $L_s = 140°$ and $L_s = 220°$ (Heyer et al., 2019), also corresponding to peak diurnal frost thickness (Piqueux et al., 2016). Heyer et al. (2019) discuss the seasonality of slope streak formation in terms of absolute peak surface temperatures, but not in terms of nighttime temperatures. Peak daytime temperatures can be associated with some of the lowest nighttime temperatures under low atmospheric aerosol opacity (Streeter et al., 2020; Wilson et al., 2006) especially at high elevation on Tharsis. The seasonality of slope streak formation relative to the presence of CO_2-ice-cold surfaces is not characterized and discussed in the literature. Future investigations with repeated seasonal coverage at other locations should be able to confirm and clarify any correlation.

Lastly, numerical simulations from Miyamoto et al. (2004) have shown that a fluidization of the avalanching material is necessary to explain the length and width of the slope streaks given the angle of the slopes on which they develop. Similarly, work by Pilorget and Forget (2015) on the formation of gullies at high latitudes, supported by Dundas et al. (2019), showed that the sublimation of seasonal CO_2 frost originally present within the pores of regolith at high latitudes created an upward gas flow leading gravity-driven avalanches to behave like liquid-fluidized flows similar to pyroclastic flows on Earth. The mechanism we propose here is comparable, as avalanching of material stirred from the warmer shallow regolith progressively covers subliming CO_2 ice downslope and promotes sublimation/fluidization. Furthermore, gas velocities reached during sublimation (Fig. 6) can be high enough to exceed the velocity threshold computed in Cedillo-Flores et al. (2011) required for fluidization of avalanching material.

This model involving carbon dioxide ice seems generally consistent with the spatio-temporal distribution of slope streaks versus diurnal CO_2 frost (Fig. 9). However, slope streaks initiate at well-defined discreet locations upslope (Schorghofer et al. (2007), Fig. 9), indicating that the conditions for their initiation are only rarely met. Otherwise, they would ubiquitously cover dusty sloped terrains and probably frequently overlap each other. For this reason, we conclude that subliming CO_2 frost alone does not seem to be sufficient to initiate slope streaks, and may need coupling with other seasonally-driven mechanisms. The interannual variability in slope streak formation rate identified by Heyer et al. (2019) is consistent with the notion that other environmental conditions may be required.

The presence of dirty diurnal CO_2 frost in the low thermal inertia terrains on Mars at low latitude is consistent with visible and thermal infrared imagery acquired at dawn. Overnight crystal growth and sublimation-driven wind have the potential to instigate grain movement. We hypothesize that diurnal CO_2 ice sublimation may be triggering and sustaining the growth of slope streaks, but other factors such as local winds may be involved in this process. Our proposed model overcomes several limitations of competing dry mechanisms presented in the literature, but it is not unequivocally validated by observations constraining the seasonality or orientation of slopes highlighted by others. Surface imaging at dawn and other local times by THEMIS and by the Colour and Stereo Surface Imaging System (CaSSIS) (Thomas et al., 2017) on the ExoMars Trace Gas Orbiter will certainly continue to provide new important constraints on the relationship between the atmosphere and the surface.

5 Conclusions

We have conducted an analysis of THEMIS visible and thermal infrared data acquired at dawn. This work constrains the relationship between diurnal frost and the surficial regolith on Mars. It unveils the potential geomorphological impact of the diurnal CO_2 cycle. Specifically:

- The distribution of THEMIS thermal infrared data acquired at dawn confirms the widespread nature of CO_2 frost on Mars previously reported (Piqueux et al., 2016; Khuller et al., 2021a), with surface temperature indicative of carbon dioxide ice presence observed at all latitudes, with a strong seasonal control;
- Multiband THEMIS visible wavelength images acquired at dawn frequently show blue/white hues interpreted as clean surface frost over a significant fraction of the surface. In the southern hemisphere, we find frosted surfaces in visible wavelength

imagery at latitudes much lower than reported in the literature, i.e., 20°S vs. 33-35°S previously. In the northern hemisphere, seasonal coverage is too sparse to precisely determine the limits of frost surface presence at THEMIS resolution;

- In the mid-to-low latitude low thermal inertia terrains (45°N-15°S), surface temperatures consistent with the presence of CO_2 frost on the ground do not show any frost signature in visible wavelength imagery. The regolith in these low thermal inertia terrains consists of 1-2 μm dust grains conducive to the formation of diurnal CO_2 ice, and we interpret the absence of frost in the visible wavelength imagery as an indication of the presence of dirty CO_2 frost forming within the surficial regolith. This conclusion is also supported by the high emissivity at 12.57 μm of these frosted surfaces;
- The dirty diurnal frost hypothesis is further supported by the notion that thermal infrared radiative cooling crucial to CO_2 frost formation peaks at a wavelength significantly longer than the regolith dust grains (18 vs $\sim$ 1 micron), thus within a layer of regolith several grains deep;
- The visible and thermal infrared observations presented in this paper could conceivably match other regolith/ice configurations and formation models than the one presented here (Fig. 1). However, the model detailed in this work is based on reasonable theoretical reasonings and is supported by our analysis;
- Within the regolith, frost sublimation-driven wind at sunrise reaches up to 3.2 cm s^{-1}, with a mean value between 1.5 and 2.0 cm s^{-1} (standard deviation of 0.8 cm s^{-1}) as a function of season, latitude, and elevation. These values are upper limits and are generally larger than (but comparable to) other values reported in the literature for seasonal ice sublimation and Knudsen pumping;
- The vertical drag exerted on individual grains can be larger and opposite in direction to cohesion plus gravity forces, suggesting that motion can be initiated by this wind. Local slope, and more importantly grain packing angle as well as cohesion forces between grains are important factors controlling whether grain motion can occur. Winds faster than 2.5 cm s^{-1} are occasionally encountered and should be able to disrupt the ground on most sloped and poorly cohesive low thermal inertia terrains;
- Recurring regolith grain movement on Mars instigated by overnight CO_2 crystal growth and rapid sublimation at sunrise could prevent the induration of the regolith observed elsewhere, maintaining large surface dust reservoirs available for lifting in the atmosphere;
- Our work supports the hypothesis that morning sublimation of diurnal CO_2 frost can initiate slope movement in low thermal inertia terrains, leading to the formation of slope streaks. Wind velocities required for fluidization are met. This hypothesis requires that slope streaks are fast forming phenomena occurring after dawn, at the colder seasons, and favoring east or equator facing slopes where early morning insolation is maximized, without the involvement of any liquid. This potential CO_2 sublimation-driven geomorphological activity occurring near the equator over short time scales would represent another expression of the complex relationship between the atmosphere and the surface;
- While slope streaks are common in low thermal inertia regions, their formation may nonetheless remain relatively rare events, otherwise they would frequently overlap each other. This observation suggests that the conditions for their formation (either initiation or development along slopes) are not often met, despite the ubiquity of CO_2 frost at the low latitude low thermal inertia terrains on Mars. Therefore, the sublimation of CO_2 frost after dawn may not be the only necessary factor required for their formation.

Surface observations at dawn are generally limited by operational constraints. Future investigations able to provide local-time-dependent characterization of the regolith will certainly help identify and characterize active processes such as the ones presented in this paper.

Open Research

All THEMIS images, TES thermal inertia map, and MOLA data are publicly available within the NASA Planetary Data System (Christensen et al., 2002; Putzig et al., 2005; Smith et al., 1999) at `https://pds-geosciences.wustl.edu/missions/odyssey/themis.html`, `https://pds-geosciences.wustl.edu/missions/mgs/tes-timap.html`, `https://pds-geosciences.wustl.edu/missions/mgs/mola.html`. The numerical model used in this paper is available at the following address: `http://krc.mars.asu.edu/`. Data files for figures and lists of THEMIS images used in this analysis are available in a public repository, see Lange et al. (2021).

Acknowledgments

Part of this work was performed at the Jet Propulsion Laboratory, California Institute of Technology under a contract with NASA. Government support acknowledged. Copyright 2022. All rights reserved. LL thanks the *Toulouse graduate School of Aerospace Engineering* and *Le Tomato* for their financial support. Suggestions from Jonathan Bapst and Kim Murray were appreciated. Part of this work was performed using JMARS. The authors appreciate constructive comments and suggestions by D.Rogers, A.Khuller, G.Portyankina, F.Schmidt, which helped improve this manuscript.

References

Aharonson, O., Schorghofer, N., & Gerstell, M. F. (2003). Slope streak formation and dust deposition rates on Mars. *Journal of Geophysical Research (Planets)*, *108*(E12), 5138. doi: 10.1029/2003JE002123

Aharonson, O., Zuber, M. T., & Rothman, D. H. (2001). Statistics of Mars' topography from the Mars Orbiter Laser Altimeter: Slopes, correlations, and physical models. , *106*(E10), 23723-23736. doi: 10.1029/2000JE001403

Appéré, T., Schmitt, B., Langevin, Y., Douté, S., Pommerol, A., Forget, F., . . . Bibring, J.-P. (2011). Winter and spring evolution of northern seasonal deposits on mars from omega on mars express. *Journal of Geophysical Research: Planets*, *116*(E5). doi: 10.1029/2010JE003762

Atwood-Stone, C., & McEwen, A. S. (2013). Avalanche slope angles in low-gravity environments from active Martian sand dunes. , *40*(12), 2929-2934. doi: 10.1002/grl.50586

Bapst, J., Bandfield, J. L., & Wood, S. E. (2015). Hemispheric asymmetry in martian seasonal surface water ice from mgs tes. *Icarus*, *260*, 396-408. doi: 10.1016/j.icarus.2015.07.025

Baratoux, D., Mangold, N., Forget, F., Cord, A., Pinet, P., Daydou, Y., . . . HRSC CO-Investigator Team (2006). The role of the wind-transported dust in slope streaks activity: Evidence from the HRSC data. , *183*(1), 30-45. doi: 10.1016/j.icarus.2006.01.023

Bennett, K. A., Hill, J. R., Murray, K. C., Edwards, C. S., Bell III, J. F., & Christensen, P. R. (2018). Themis-vis investigations of sand at gale crater. *Earth and Space Science*, *5*(8), 352-363. doi: 10.1029/2018EA000380

Bhardwaj, A., Sam, L., Martín-Torres, F. J., & Zorzano, M.-P. (2019). Are slope streaks indicative of global-scale aqueous processes on contemporary mars? *Reviews of Geophysics*, *57*(1), 48-77. doi: 10.1029/2018RG000617

Bibring, J. P., Soufflot, A., Berthé, M., Langevin, Y., Gondet, B., Drossart, P., . . . Forget, F. (2004). OMEGA: Observatoire pour la Minéralogie, l'Eau, les Glaces et l'Activité. In A. Wilson & A. Chicarro (Eds.), *Mars express: the*

scientific payload (Vol. 1240, p. 37-49).
Brusnikin, E. S., Kreslavsky, M. A., Zubarev, A. E., Patratiy, V. D., Krasilnikov, S. S., Head, J. W., & Karachevtseva, I. P. (2016). Topographic measurements of slope streaks on mars. , *278*, 52–61. doi: 10.1016/j.icarus.2016.06.005
Brutsaert, W. (1982). The lower atmosphere. In (pp. 37–56). Springer Netherlands. doi: 10.1007/978-94-017-1497-6_3
Burleigh, K. J., Melosh, H. J., Tornabene, L. L., Ivanov, B., McEwen, A. S., & Daubar, I. J. (2012). Impact airblast triggers dust avalanches on mars. , *217*(1), 194–201. doi: 10.1016/j.icarus.2011.10.026
Calvin, W., Cantor, B., & James, P. (2017). Interannual and seasonal changes in the south seasonal polar cap of mars: Observations from my 28-31 using marci. *Icarus*, *292*, 144-153. doi: 10.1016/j.icarus.2017.01.010
Calvin, W., James, P., Cantor, B., & Dixon, E. (2015). Interannual and seasonal changes in the north polar ice deposits of mars: Observations from my 29–31 using marci. *Icarus*, *251*, 181-190. (Dynamic Mars) doi: 10.1016/j.icarus.2014.08.026
Cedillo-Flores, Y., Treiman, A. H., Lasue, J., & Clifford, S. M. (2011). Co2 gas fluidization in the initiation and formation of martian polar gullies. *Geophysical Research Letters*, *38*(21). doi: 10.1029/2011GL049403
Christensen, P., Gorelick, N., Mehall, G., & Murray, K. (2002). 2001 mars odyssey thermal emission imaging system visible geometrically registered data product.
Christensen, P. R., Bandfield, J. L., Hamilton, V. E., Ruff, S. W., Kieffer, H. H., Titus, T. N., ... Greenfield, M. (2001). Mars global surveyor thermal emission spectrometer experiment: Investigation description and surface science results. , *106*(E10), 23823–23871. doi: 10.1029/2000je001370
Christensen, P. R., & Harrison, S. T. (1993). Thermal infrared emission spectroscopy of natural surfaces: Application to desert varnish coatings on rocks. , *98*(B11), 19819–19834. doi: 10.1029/93jb00135
Christensen, P. R., Jakosky, B. M., Kieffer, H. H., Malin, M. C., Jr, H. Y. M., Nealson, K., ... Ravine, M. (2004). The thermal emission imaging system (themis) for the mars 2001 odyssey mission. In (pp. 85–130). Springer Netherlands. doi: 10.1007/978-0-306-48600-5_3
Chuang, F. C., Beyer, R. A., & Bridges, N. T. (2010). Modification of martian slope streaks by eolian processes. , *205*(1), 154–164. doi: 10.1016/j.icarus.2009.07.035
Chuang, F. C., Beyer, R. A., McEwen, A. S., & Thomson, B. J. (2007). HiRISE observations of slope streaks on mars. , *34*(20). doi: 10.1029/2007gl031111
Colaprete, A., & Toon, O. B. (2002). Carbon dioxide snow storms during the polar night on mars. *Journal of Geophysical Research: Planets*, *107*(E7), 5-1-5-16. doi: 10.1029/2001JE001758
de Beule, C., Wurm, G., Kelling, T., Küpper, M., Jankowski, T., & Teiser, J. (2013). The martian soil as a planetary gas pump. , *10*(1), 17–20. doi: 10.1038/nphys2821
Diniega, S., Bramson, A. M., Buratti, B., Buhler, P., Burr, D. M., Chojnacki, M., ... Widmer, J. M. (2021). Modern mars' geomorphological activity, driven by wind, frost, and gravity. , *380*, 107627. doi: 10.1016/j.geomorph.2021.107627
Diniega, S., Hansen, C., McElwaine, J., Hugenholtz, C., Dundas, C., McEwen, A., & Bourke, M. (2013). A new dry hypothesis for the formation of martian linear gullies. , *225*(1), 526–537. doi: 10.1016/j.icarus.2013.04.006
Dundas, C. M. (2020). Geomorphological evidence for a dry dust avalanche origin of slope streaks on mars. , *13*(7), 473–476. doi: 10.1038/s41561-020-0598-x
Dundas, C. M., Diniega, S., Hansen, C. J., Byrne, S., & McEwen, A. S. (2012). Seasonal activity and morphological changes in martian gullies. , *220*(1), 124–143. doi: 10.1016/j.icarus.2012.04.005

Dundas, C. M., McEwen, A. S., Diniega, S., Hansen, C. J., Byrne, S., & McElwaine, J. N. (2019). The formation of gullies on Mars today. In *Martian Gullies and their Earth Analogues.* Geological Society of London. doi: 10.1144/SP467.5

Edwards, C. S., Nowicki, K. J., Christensen, P. R., Hill, J., Gorelick, N., & Murray, K. (2011). Mosaicking of global planetary image datasets: 1. techniques and data processing for thermal emission imaging system (THEMIS) multi-spectral data. , *116*(E10). doi: 10.1029/2010je003755

Everett, D. H. (1961). The thermodynamics of frost damage to porous solids. , *57*, 1541. doi: 10.1039/tf9615701541

Ferris, J. C., Dohm, J. M., Baker, V. R., & Maddock, T. (2002). Dark slope streaks on mars: Are aqueous processes involved? , *29*(10), 128–1–128–4. doi: 10.1029/2002gl014936

Forget, F., Hansen, G. B., & Pollack, J. B. (1995). Low brightness temperatures of martian polar caps: CO2clouds or low surface emissivity? , *100*(E10), 21219. doi: 10.1029/95je02378

Forget, F., Hourdin, F., & Talagrand, O. (1998). Co_2 snowfall on mars: Simulation with a general circulation model. *Icarus*, *131*(2), 302-316. doi: 10.1006/icar.1997.5874

Forget, F., & Pollack, J. B. (1996). Thermal infrared observations of the condensing martian polar caps: Co2 ice temperatures and radiative budget. *Journal of Geophysical Research: Planets*, *101*(E7), 16865-16879. doi: 10.1029/96JE01077

Goetz, W., Hviid, S., Madsen, M., & Kinch, K. (2008). Magnetic properties results from martian surface landers and rovers. In J. Bell (Ed.), *The martian surface:*. United Kingdom: Cambridge University Press.

Greeley, R. (2002). Saltation impact as a means for raising dust on mars. *Planetary and Space Science*, *50*(2), 151-155. doi: 10.1016/S0032-0633(01)00127-1

Greeley, R., Lancaster, N., Lee, S., & Thomas, P. (1992). Martian aeolian processes, sediments, and features. In M. George (Ed.), *Mars* (p. 730-766).

Greeley, R., Leach, R., White, B., Iversen, J., & Pollack, J. B. (1980). Threshold windspeeds for sand on Mars: Wind tunnel simulations. , *7*(2), 121-124. doi: 10.1029/GL007i002p00121

Greeley, R., White, B., Leach, R., Iversen, J., & Pollack, J. (1976). Mars: Wind friction speeds for particle movement. *Geophysical Research Letters*, *3*(8), 417-420. doi: 10.1029/GL003i008p00417

Greenberg, J. M., Mizutani, H., & Yamamoto, T. (1995). A new derivation of the tensile strength of cometary nuclei: application to comet Shoemaker-Levy 9. , *295*, L35-L38.

Grott, M., Helbert, J., & Nadalini, R. (2007). Thermal structure of martian soil and the measurability of the planetary heat flow. *Journal of Geophysical Research: Planets*, *112*(E9). doi: 10.1029/2007JE002905

Haberle, R. M. (1979). The influence of the Martian polar caps on the diurnal tide. , *39*(2), 184-191. doi: 10.1016/0019-1035(79)90162-3

Haberle, R. M., Leovy, C. B., & Pollack, J. B. (1979). A numerical model of the martian polar cap winds. *Icarus*, *39*(2), 151-183. doi: 10.1016/0019-1035(79)90161-1

Hansen, C., Byrne, S., Portyankina, G., Bourke, M., Dundas, C., McEwen, A., ... Thomas, N. (2013). Observations of the northern seasonal polar cap on mars: I. spring sublimation activity and processes. , *225*(2), 881–897. doi: 10.1016/j.icarus.2012.09.024

Hansen, C., Thomas, N., Portyankina, G., McEwen, A., Becker, T., Byrne, S., ... Mellon, M. (2010). HiRISE observations of gas sublimation-driven activity in mars' southern polar regions: I. erosion of the surface. , *205*(1), 283–295. doi: 10.1016/j.icarus.2009.07.021

Hansen, G. B. (1997). The infrared absorption spectrum of carbon dioxide ice from

1.8 to 333 µm. *Journal of Geophysical Research: Planets*, *102*(E9), 21569-21587. doi: 10.1029/97JE01875

Hartzell, C., Wang, X., Scheeres, D., & Horányi, M. (2013). Experimental demonstration of the role of cohesion in electrostatic dust lofting. , *40*(6), 1038–1042. doi: 10.1002/grl.50230

Hayne, P. O., Paige, D. A., & Heavens, N. G. (2014). The role of snowfall in forming the seasonal ice caps of mars: Models and constraints from the mars climate sounder. *Icarus*, *231*, 122-130. doi: 10.1016/j.icarus.2013.10.020

Hayne, P. O., Paige, D. A., Schofield, J. T., Kass, D. M., Kleinböhl, A., Heavens, N. G., & McCleese, D. J. (2012). Carbon dioxide snow clouds on mars: South polar winter observations by the mars climate sounder. , *117*(E8). doi: 10.1029/2011je004040

Henderson, B. G., & Jakosky, B. M. (1994). Near-surface thermal gradients and their effects on mid-infrared emission spectra of planetary surfaces. , *99*(E9), 19063-19074. doi: 10.1029/94JE01861

Heyer, T., Kreslavsky, M., Hiesinger, H., Reiss, D., Bernhardt, H., & Jaumann, R. (2019). Seasonal formation rates of martian slope streaks. , *323*, 76–86. doi: 10.1016/j.icarus.2019.01.010

Hourdin, F., Van, P. L., Forget, F., & Talagrand, O. (1993). Meteorological variability and the annual surface pressure cycle on mars. , *50*(21), 3625–3640. doi: 10.1175/1520-0469(1993)050<3625:mvatas>2.0.co;2

Hu, R. (2019). Predicted diurnal variation of the deuterium to hydrogen ratio in water at the surface of mars caused by mass exchange with the regolith. *Earth and Planetary Science Letters*, *519*, 192-201. doi: 10.1016/j.epsl.2019.05.017

Jakosky, B. M., & Christensen, P. R. (1986). Global duricrust on mars: Analysis of remote-sensing data. , *91*(B3), 3547–3559. doi: 10.1029/jb091ib03p03547

James, P. B., Kieffer, H. H., & Paige, D. A. (1992). The seasonal cycle of carbon dioxide on Mars. In M. George (Ed.), *Mars* (p. 934-968).

Johnson, J. R., Christensen, P. R., & Lucey, P. G. (2002). Dust coatings on basaltic rocks and implications for thermal infrared spectroscopy of mars. *Journal of Geophysical Research E: Planets*, *107*(E6), 2-1-2-19. Retrieved from `http://pubs.er.usgs.gov/publication/70024522` doi: 10.1029/2000JE001405

Khuller, A. R., Christensen, P. R., Harrison, T. N., & Diniega, S. (2021a). The distribution of frosts on mars: Links to present-day gully activity. *Journal of Geophysical Research: Planets*, *126*(3), e2020JE006577. doi: 10.1029/2020JE006577

Khuller, A. R., Christensen, P. R., & Warren, S. G. (2021b). Spectral albedo of dusty martian h2o snow and ice. *Journal of Geophysical Research: Planets*, *126*(9), e2021JE006910. doi: 10.1029/2021JE006910

Kieffer, H. H. (1968). *Near infrared spectral reflectance of simulated Martian frosts* (Doctoral dissertation, California Institute of Technology, United States). doi: 10.7907/BHED-BJ17

Kieffer, H. H. (2001). TES mapping of mars' north seasonal cap. , *154*(1), 162–180. doi: 10.1006/icar.2001.6670

Kieffer, H. H. (2007). Cold jets in the martian polar caps. , *112*(E8). doi: 10.1029/2006je002816

Kieffer, H. H. (2013). Thermal model for analysis of mars infrared mapping. , *118*(3), 451–470. doi: 10.1029/2012je004164

Kieffer, H. H., Christensen, P. R., & Titus, T. N. (2006). CO2 jets formed by sublimation beneath translucent slab ice in mars' seasonal south polar ice cap. , *442*(7104), 793–796. doi: 10.1038/nature04945

Kieffer, H. H., Titus, T. N., Mullins, K. F., & Christensen, P. R. (2000). Mars south polar spring and summer behavior observed by TES: Seasonal cap evolution controlled by frost grain size. , *105*(E4), 9653–9699. doi: 10.1029/1999je001136

Kinch, K. M., Bell, J. F., Goetz, W., Johnson, J. R., Joseph, J., Madsen, M. B., & Sohl-Dickstein, J. (2015). Dust deposition on the decks of the mars exploration rovers: 10 years of dust dynamics on the panoramic camera calibration targets. , *2*(5), 144–172. doi: 10.1002/2014ea000073

Kinch, K. M., Merrison, J. P., Gunnlaugsson, H. P., Bertelsen, P., Madsen, M. B., & Nørnberg, P. (2006). Preliminary analysis of the MER magnetic properties experiment using a computational fluid dynamics model. , *54*(1), 28-44. doi: 10.1016/j.pss.2005.07.008

Kleinhans, M. G., Markies, H., de Vet, S. J., in 't Veld, A. C., & Postema, F. N. (2011). Static and dynamic angles of repose in loose granular materials under reduced gravity. *Journal of Geophysical Research: Planets*, *116*(E11). doi: 10.1029/2011JE003865

Kreslavsky, M. A., & Head, J. W. (1999). Kilometer-scale slopes on mars and their correlation with geologic units: Initial results from mars orbiter laser altimeter (mola) data. *Journal of Geophysical Research: Planets*, *104*(E9), 21911-21924. doi: 10.1029/1999JE001051

Kreslavsky, M. A., & Head, J. W. (2000). Kilometer-scale roughness of Mars: Results from MOLA data analysis. , *105*(E11), 26695-26712. doi: 10.1029/2000JE001259

Kreslavsky, M. A., & Head, J. W. (2009). Slope streaks on mars: A new "wet" mechanism. , *201*(2), 517–527. doi: 10.1016/j.icarus.2009.01.026

Lange, L., Piqueux, S., & Edwards, C. S. (2021). *Gardening of the Martian Regolith by Diurnal CO2 Frost and the Formation of Slope Streaks.* Harvard Dataverse. doi: 10.7910/DVN/AUWKSB

Langevin, Y., Douté, S., Vincendon, M., Poulet, F., Bibring, J.-P., Gondet, B., ... Forget, F. (2006). No signature of clear CO2 ice from the 'cryptic' regions in mars' south seasonal polar cap. , *442*(7104), 790–792. doi: 10.1038/nature05012

Leighton, R. B., & Murray, B. C. (1966). Behavior of carbon dioxide and other volatiles on mars. , *153*(3732), 136–144. doi: 10.1126/science.153.3732.136

Lemmon, M. T., Guzewich, S. D., McConnochie, T., Vicente-Retortillo, A., Martínez, G., Smith, M. D., ... Jacob, S. (2019). Large dust aerosol sizes seen during the 2018 martian global dust event by the curiosity rover. , *46*(16), 9448–9456. doi: 10.1029/2019gl084407

Mahaffy, P. R., Webster, C. R., Atreya, S. K., Franz, H., Wong, M., Conrad, P. G., ... and, J. E. M. (2013). Abundance and isotopic composition of gases in the martian atmosphere from the curiosity rover. , *341*(6143), 263–266. doi: 10.1126/science.1237966

Mangan, T., Salzmann, C., Plane, J., & Murray, B. (2017). CO2 ice structure and density under martian atmospheric conditions. , *294*, 201–208. doi: 10.1016/j.icarus.2017.03.012

Martínez, G., Fischer, E., Rennó, N., Sebastián, E., Kemppinen, O., Bridges, N., ... Gómez-Elvira, J. (2016). Likely frost events at gale crater: Analysis from msl/rems measurements. *Icarus*, *280*, 93-102. (MicroMars to MegaMars) doi: 10.1016/j.icarus.2015.12.004

McCleese, D. J., Schofield, J. T., Taylor, F. W., Calcutt, S. B., Foote, M. C., Kass, D. M., ... Zurek, R. W. (2007). Mars climate sounder: An investigation of thermal and water vapor structure, dust and condensate distributions in the atmosphere, and energy balance of the polar regions. , *112*(E5). doi: 10.1029/2006je002790

McEwen, A. S., Hansen, C. J., Delamere, W. A., Eliason, E. M., Herkenhoff, K. E., Keszthelyi, L., ... Wray, J. J. (2007). A closer look at water-related geologic activity on mars. *Science*, *317*(5845), 1706-1709. doi: 10.1126/science.1143987

McEwen, A. S., Ojha, L., Dundas, C. M., Mattson, S. S., Byrne, S., Wray, J. J.,

... Gulick, V. C. (2011). Seasonal flows on warm martian slopes. *Science*, *333*(6043), 740-743. doi: 10.1126/science.1204816

Mellon, M. T., Jakosky, B. M., Kieffer, H. H., & Christensen, P. R. (2000). High-resolution thermal inertia mapping from the mars global surveyor thermal emission spectrometer. *Icarus*, *148*(2), 437-455. doi: 10.1006/icar.2000.6503

Merrison, J., Gunnlaugsson, H., Nørnberg, P., Jensen, A., & Rasmussen, K. (2007). Determination of the wind induced detachment threshold for granular material on mars using wind tunnel simulations. *Icarus*, *191*(2), 568-580. doi: 10.1016/j.icarus.2007.04.035

Mischna, M. A., & Piqueux, S. (2020). The role of atmospheric pressure on mars surface properties and early mars climate modeling. , *342*, 113496. doi: 10.1016/j.icarus.2019.113496

Miyamoto, H., Dohm, J. M., Beyer, R. A., & Baker, V. R. (2004). Fluid dynamical implications of anastomosing slope streaks on mars. *Journal of Geophysical Research: Planets*, *109*(E6). doi: 10.1029/2003JE002234

Murchie, S. L., Bibring, J.-P., Arvidson, R. E., Bishop, J. L., Carter, J., Ehlmann, B. L., ... Viviano, C. E. (2019). Visible to short-wave infrared spectral analyses of mars from orbit using CRISM and OMEGA. In (pp. 453–483). Cambridge University Press. doi: 10.1017/9781316888872.025

Murray, K. C., Christensen, P. R., & Mehall, G. L. (2016). Themis geometric processing user's guide.

Mushkin, A., Gillespie, A. R., Montgomery, D. R., Schreiber, B. C., & Arvidson, R. E. (2010). Spectral constraints on the composition of low-albedo slope streaks in the olympus mons aureole. , *37*(22). doi: 10.1029/2010gl044535

Owen, T., Biemann, K., Rushneck, D. R., Biller, J. E., Howarth, D. W., & Lafleur, A. L. (1977). The composition of the atmosphere at the surface of mars. *Journal of Geophysical Research (1896-1977)*, *82*(28), 4635-4639. doi: 10.1029/JS082i028p04635

Perko, H. A., Nelson, J. D., & Green, J. R. (2002). Review of martian dust composition, transport, deposition, adhesion, and removal. American Society of Civil Engineers. doi: 10.1061/40625(203)25

Perko, H. A., Nelson, J. D., & Sadeh, W. Z. (2001). Surface cleanliness effect on lunar soil shear strength. , *127*(4), 371–383. doi: 10.1061/(asce)1090-0241(2001)127:4(371)

Phillips, C., Burr, D., & Beyer, R. (2007). Mass movement within a slope streak on mars. *Geophys. Res. Lett*, *34*. doi: 10.1029/2007GL031577

Phillips, M. (1980). A force balance model for particle entrainment into a fluid stream. , *13*(2), 221–233. doi: 10.1088/0022-3727/13/2/019

Pilorget, C., Edwards, C. S., Ehlmann, B. L., Forget, F., & Millour, E. (2013). Material ejection by the cold jets and temperature evolution of the south seasonal polar cap of mars from THEMIS/CRISM observations and implications for surface properties. , *118*(12), 2520–2536. doi: 10.1002/2013je004513

Pilorget, C., & Forget, F. (2015). Formation of gullies on mars by debris flows triggered by CO2 sublimation. , *9*(1), 65–69. doi: 10.1038/ngeo2619

Pilorget, C., Forget, F., Millour, E., Vincendon, M., & Madeleine, J. (2011). Dark spots and cold jets in the polar regions of mars: New clues from a thermal model of surface CO2 ice. , *213*(1), 131–149. doi: 10.1016/j.icarus.2011.01.031

Piqueux, S., Byrne, S., & Richardson, M. I. (2003). Sublimation of mars's southern seasonal co2 ice cap and the formation of spiders. *Journal of Geophysical Research: Planets*, *108*(E8). doi: 10.1029/2002JE002007

Piqueux, S., & Christensen, P. R. (2008). North and south subice gas flow and venting of the seasonal caps of mars: A major geomorphological agent. , *113*(E6). doi: 10.1029/2007je003009

Piqueux, S., & Christensen, P. R. (2009a). A model of thermal conductivity for planetary soils: 1. theory for unconsolidated soils. , *114*(E9). doi: 10.1029/2008je003308

Piqueux, S., & Christensen, P. R. (2009b). A model of thermal conductivity for planetary soils: 2. theory for cemented soils. , *114*(E9). doi: 10.1029/2008je003309

Piqueux, S., Edwards, C. S., & Christensen, P. R. (2008). Distribution of the ices exposed near the south pole of mars using thermal emission imaging system (THEMIS) temperature measurements. , *113*(E8). doi: 10.1029/2007je003055

Piqueux, S., Kleinböhl, A., Hayne, P. O., Heavens, N. G., Kass, D. M., McCleese, D. J., … Shirley, J. H. (2016). Discovery of a widespread low-latitude diurnal CO2 frost cycle on mars. , *121*(7), 1174–1189. doi: 10.1002/2016je005034

Piqueux, S., Kleinböhl, A., Hayne, P. O., Kass, D. M., Schofield, J. T., & McCleese, D. J. (2015). Variability of the martian seasonal CO2 cap extent over eight mars years. , *251*, 164–180. doi: 10.1016/j.icarus.2014.10.045

Pommerol, A., Appéré, T., Portyankina, G., Aye, K.-M., Thomas, N., & Hansen, C. (2013). Observations of the northern seasonal polar cap on mars III: CRISM/HiRISE observations of spring sublimation. , *225*(2), 911–922. doi: 10.1016/j.icarus.2012.08.039

Pommerol, A., Portyankina, G., Thomas, N., Aye, K. M., Hansen, C. J., Vincendon, M., & Langevin, Y. (2011). Evolution of south seasonal cap during Martian spring: Insights from high-resolution observations by HiRISE and CRISM on Mars Reconnaissance Orbiter. *Journal of Geophysical Research (Planets)*, *116*(E8), E08007. doi: 10.1029/2010JE003790

Portyankina, G., Markiewicz, W. J., Thomas, N., Hansen, C. J., & Milazzo, M. (2010). HiRISE observations of gas sublimation-driven activity in mars' southern polar regions: III. models of processes involving translucent ice. , *205*(1), 311–320. doi: 10.1016/j.icarus.2009.08.029

Portyankina, G., Pommerol, A., Aye, K.-M., Hansen, C. J., & Thomas, N. (2012). Polygonal cracks in the seasonal semi-translucent CO2ice layer in martian polar areas. , *117*(E2). doi: 10.1029/2011je003917

Presley, M., & Christensen, P. (1997). Thermal conductivity measurements of particulate materials 2. results. *Journal of Geophysical Research*, *102*, 6551-6566. doi: 10.1029/96JE03303

Putzig, N. E., Mellon, M. T., Kretke, K. A., & Arvidson, R. E. (2005). Global thermal inertia and surface properties of mars from the mgs mapping mission. *Icarus*, *173*(2), 325-341. doi: 10.1016/j.icarus.2004.08.017

Ramsey, M. S., & Christensen, P. R. (1992). The Linear "Un-Mixing" of Laboratory Thermal Infrared Spectra: Implications for the Thermal Emission Spectrometer (TES) Experiment, Mars Observer. In *Lunar and planetary science conference* (Vol. 23, p. 1127).

Ruedrich, J., & Siegesmund, S. (2006). Salt and ice crystallisation in porous sandstones. , *52*(2), 225–249. doi: 10.1007/s00254-006-0585-6

Ruff, S. W., & Christensen, P. R. (2002). Bright and dark regions on mars: Particle size and mineralogical characteristics based on thermal emission spectrometer data. , *107*(E12), 2–1–2–22. doi: 10.1029/2001je001580

Scheeres, D., Hartzell, C., Sánchez, P., & Swift, M. (2010). Scaling forces to asteroid surfaces: The role of cohesion. , *210*(2), 968–984. doi: 10.1016/j.icarus.2010.07.009

Schmidt, F., Andrieu, F., Costard, F., Kocifaj, M., & Meresescu, A. G. (2017). Formation of recurring slope lineae on mars by rarefied gas-triggered granular flows. , *10*(4), 270–273. doi: 10.1038/ngeo2917

Schmitt, B., Quirico, E., Trotta, F., & Grundy, W. M. (1998). Optical properties of ices from uv to infrared. In B. Schmitt, C. De Bergh, & M. Festou (Eds.), *Solar system ices: Based on reviews presented at the international symposium "solar system ices" held in toulouse, france, on march 27–30, 1995* (p. 199-

240). Dordrecht: Springer Netherlands. doi: 10.1007/978-94-011-5252-5_9

Schorghofer, N., Aharonson, O., Gerstell, M., & Tatsumi, L. (2007). Three decades of slope streak activity on mars. *Icarus*, *191*, 132-140. doi: 10.1016/j.icarus.2007.04.026

Schorghofer, N., Aharonson, O., & Khatiwala, S. (2002). Slope streaks on mars: Correlations with surface properties and the potential role of water. , *29*(23), 41–1–41–4. doi: 10.1029/2002gl015889

Schorghofer, N., & Edgett, K. (2006). Seasonal surface frost at low latitudes on mars. *Icarus*, *180*, 321-334. doi: 10.1016/j.icarus.2005.08.022

Schorghofer, N., & King, C. M. (2011). Sporadic formation of slope streaks on mars. , *216*(1), 159–168. doi: 10.1016/j.icarus.2011.08.028

Sears, W. R. (1981). Classical aerodynamic theory. compiled by robert t. jones. nasa reference publiation no. 1050, 1979, 311 pp. from national technical information service, springfield, va 22161. *Journal of Fluid Mechanics*, *102*, 473–475. doi: 10.1017/S0022112081222743

Singh, D., & Flanner, M. G. (2016). An improved carbon dioxide snow spectral albedo model: Application to martian conditions. , *121*(10), 2037–2054. doi: 10.1002/2016je005040

Smith, D., Neumann, G., Ford, P., Arvidson, R. E., Guinness, E. A., & Slavney, S. (1999). Mars global surveyor laser altimeter precision experiment data record.

Sprague, A. L., Boynton, W. V., Kerry, K. E., Janes, D. M., Hunten, D. M., Kim, K. J., ... Metzger, A. E. (2004). Mars' south polar ar enhancement: A tracer for south polar seasonal meridional mixing. , *306*(5700), 1364–1367. doi: 10.1126/science.1098496

Sprague, A. L., Boynton, W. V., Kerry, K. E., Janes, D. M., Kelly, N. J., Crombie, M. K., ... Metzger, A. E. (2007). Mars' atmospheric argon: Tracer for understanding martian atmospheric circulation and dynamics. , *112*(E3). doi: 10.1029/2005je002597

Streeter, P. M., Lewis, S. R., Patel, M. R., Holmes, J. A., & Kass, D. M. (2020). Surface warming during the 2018/mars year 34 global dust storm. *Geophysical Research Letters*, *47*(9), e2019GL083936. (e2019GL083936 2019GL083936) doi: 10.1029/2019GL083936

Sullivan, R., Arvidson, R., Bell, J. F., Gellert, R., Golombek, M., Greeley, R., ... Wray, J. (2008). Wind-driven particle mobility on mars: Insights from mars exploration rover observations at "el dorado" and surroundings at gusev crater. , *113*(E6). doi: 10.1029/2008je003101

Sullivan, R., Thomas, P., Veverka, J., Malin, M., & Edgett, K. (2001). Mass movement slope streaks imaged by the mars orbiter camera. *The Journal of Geophysical Research Planets*, *106*, 23,607–23,633. doi: 10.1029/2000JE001296

Svitek, T., & Murray, B. C. (1990). Winter frost at viking lander 2 site. *Journal of Geophysical Research*, *95*, 1495-1510.

Sylvest, M. E., Dixon, J. C., Conway, S. J., Patel, M. R., McElwaine, J. N., Hagermann, A., & Barnes, A. (2018). CO2 sublimation in martian gullies: laboratory experiments at varied slope angle and regolith grain sizes. , *467*(1), 343–371. doi: 10.1144/sp467.11

Thomas, N., Cremonese, G., Ziethe, R., Gerber, M., Brändli, M., Bruno, G., ... Wray, J. J. (2017). The colour and stereo surface imaging system (CaSSIS) for the ExoMars trace gas orbiter. , *212*(3-4), 1897–1944. doi: 10.1007/s11214-017-0421-1

Thomas, N., Hansen, C., Portyankina, G., & Russell, P. (2010). HiRISE observations of gas sublimation-driven activity in mars' southern polar regions: II. surficial deposits and their origins. , *205*(1), 296–310. doi: 10.1016/j.icarus.2009.05.030

Titus, T. N., Calvin, W. M., Kieffer, H. H., Langevin, Y., & Prettyman, T. H. (2008). Martian polar processes. In J. Bell (Ed.), *The martian surface:*

Composition, mineralogy and physical properties (p. 578–598). Cambridge University Press. doi: 10.1017/CBO9780511536076.026

Vincendon, M., Mustard, J., Forget, F., Kreslavsky, M., Spiga, A., Murchie, S., & Bibring, J.-P. (2010). Near-tropical subsurface ice on mars. , *37*(1). doi: 10.1029/2009gl041426

Warren, S. G., Wiscombe, W. J., & Firestone, J. F. (1990). Spectral albedo and emissivity of CO2in martian polar caps: Model results. , *95*(B9), 14717. doi: 10.1029/jb095ib09p14717

Wilson, R. J., Neumann, G. A., & Smith, M. D. (2006). Diurnal variation and radiative influence of martian water ice clouds. *Geophysical Research Letters*, *34*.

Withers, P. (2012). Empirical estimates of martian surface pressure in support of the landing of mars science laboratory. , *170*(1-4), 837–860. doi: 10.1007/s11214-012-9876-2

Wolff, M. J., Smith, M. D., Clancy, R. T., Spanovich, N., Whitney, B. A., Lemmon, M. T., ... Squyres, S. W. (2006). Constraints on dust aerosols from the mars exploration rovers using mgs overflights and mini-tes. *Journal of Geophysical Research: Planets*, *111*(E12). doi: 10.1029/2006JE002786

Woronko, B., & Pisarska-Jamroży, M. (2015). Micro-scale frost weathering of sand-sized quartz grains. , *27*(1), 109–122. doi: 10.1002/ppp.1855

Yang, H., Fan, M., Liu, A., & Dong, L. (2015). General formulas for drag coefficient and settling velocity of sphere based on theoretical law. , *25*(2), 219–223. doi: 10.1016/j.ijmst.2015.02.009

Zuber, M. T., Smith, D. E., Solomon, S. C., Muhleman, D. O., Head, J. W., Garvin, J. B., ... Bufton, J. L. (1992). The mars observer laser altimeter investigation. *Journal of Geophysical Research: Planets*, *97*(E5), 7781-7797. doi: 10.1029/92JE00341

Journal of Geophysical Research: Planets

Supporting Information for

Gardening of the Martian Regolith by Diurnal CO_2 Frost and the Formation of Slope Streaks

L.Lange[1,2], S.Piqueux[3], and C.S.Edwards[4]

[1]SSPA, Institut Supérieur de l'Aéronautique et de l'Espace (ISAE-SUPAERO), Université de Toulouse, 31400, Toulouse, France

[2]Laboratoire de Météorologie Dynamique, Institut Pierre-Simon Laplace (LMD/IPSL), Sorbonne Université, Centre National de la Recherche Scientifique (CNRS), École Polytechnique, École Normale Supérieure (ENS), Paris, France

[3]Jet Propulsion Laboratory, California Institute of Technology, Pasadena, CA 91109, USA

[4]Northern Arizona University, Department of Astronomy and Planetary Science PO BOX 6010 Flagstaff, AZ 86011, USA

Contents of this file

Figures S1

Introduction

This document presents a figure illustrating the distribution of THEMIS images indicative of the presence of CO_2 ice (i.e., within 5K of the local CO_2 frost point) and documents the frost identification confidence level (Class 1-5) following a classification described in section 2.2.

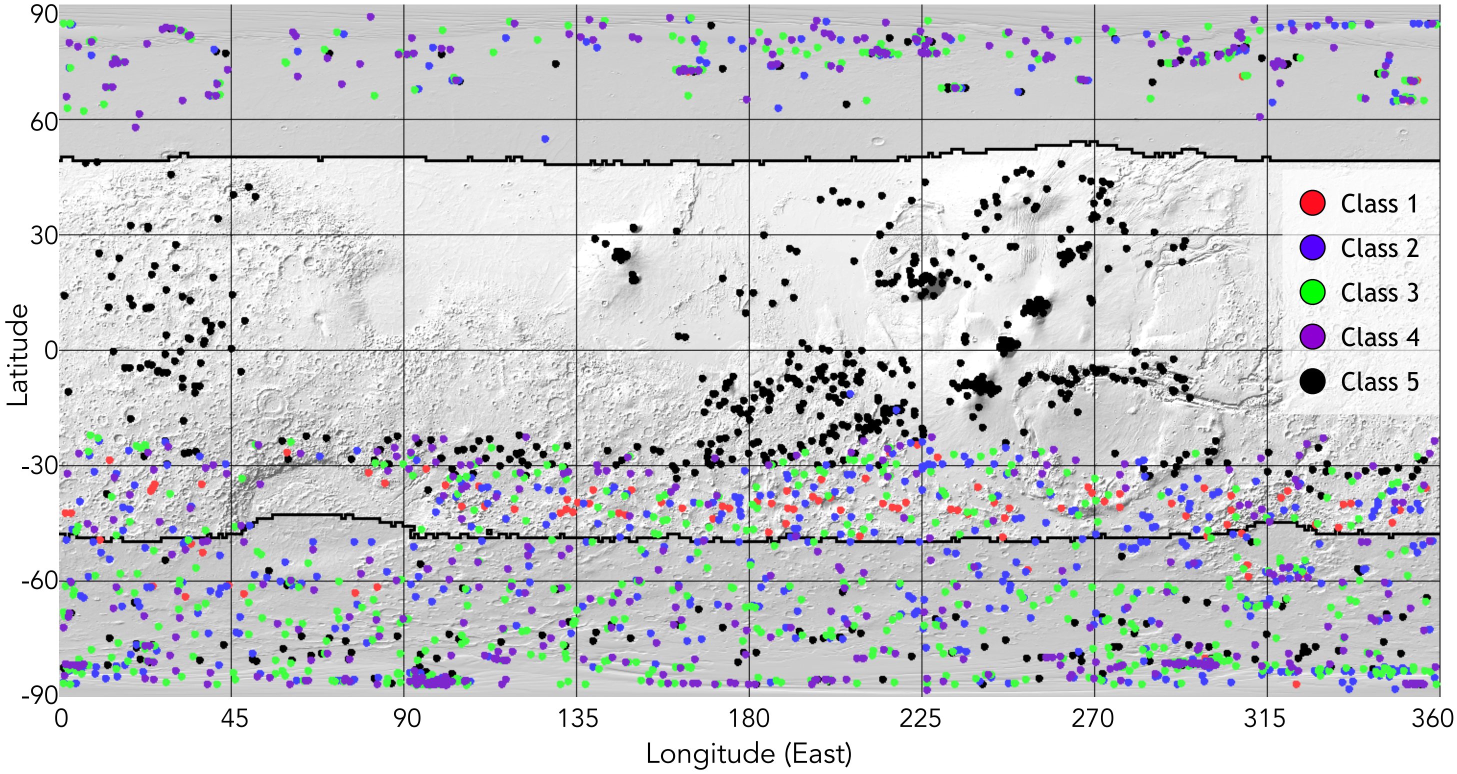

Figure S1. Distribution of THEMIS visible and infrared wavelength image pairs within 5 K of the local CO_2 frost point, near sun rise. The color of the dots indicates the confidence level of the frost identification in the THEMIS visible wavelengths images: red for Class 1 images (115 occurrences), blue for Class 2 images (534 occurrences), green for Class 3 images (708 occurrences), purple for Class 4 images (556 occurrences), black for Class 5 (848 occurrences). Grey background is a MOLA-shaded relief map. Maximum extent of the seasonal caps (Piqueux et al., 2015) shown as black curves.